12-2009

Spatial Frequency Localization in Mammograms Using Wavelets

Tomislav Bujanovic
Western Michigan University

SPATIAL FREQUENCY LOCALIZATION IN MAMMOGRAMS USING WAVELETS

by

Tomislav Bujanovic

A Dissertation
Submitted to the
Faculty of The Graduate College
in partial fulfillment of the
requirements for the
Degree of Doctor of Philosophy
Department of Electrical and Computer Engineering
Advisor: Ikhlas Abdel-Qader, Ph.D.

Western Michigan University
Kalamazoo, Michigan
December 2009

SPATIAL FREQUENCY LOCALIZATION IN MAMMOGRAMS USING WAVELETS

Tomislav Bujanovic, Ph.D.

Western Michigan University, 2009

Microcalcifications are residual calcium deposits that are often the first signs of developing breast abnormalities that may lead to breast cancer. Up to 30% of cancerous lesion in diagnosed breast cancer cases could have been detected earlier through mammogram screenings if the right tools were available. While the detection of calcifications may be easier in fatty backgrounds, it is challenging in dense parenchyma, suggesting the need for more sensitive tools for accurately identifying suspicious regions in mammograms and propping a computer-aided system for further target classification. Therefore, the objective of the research work in this dissertation is to develop a novel highly sensitive method for the detection of microcalcification that is independent of the characteristics of background tissue.

Continuous wavelet transform is employed to detect singularities in mammograms by tracking modulus maxima along maxima lines. This work is based on convolving the mammogram with Gaussian kernel to detect and extract microcalcifications that are modeled as smoothed impulse functions. Two significant characteristics of the local modulus maxima of the wavelet transform with respect to the smoothed impulse function are investigated: magnitude of general maximum and fractal dimension of the detected sets of singularities. It is also essential to select the

suitable computation parameters such as thresholds of magnitude, argument, and frequency range in accordance with spatial and numerical resolution of the analyzed mammogram. This detection approach is independent of the background tissue and is complementary to a computer-aided diagnosis system based on shape, morphology, and spatial distribution of individual microcalcifications.

Experimental work is performed on a set of images with empirically selected parameters for 200 μm/pixel spatial and 8 bits/pixel numerical resolution. Results are indicating that in abnormal regions the selected general maxima have larger magnitudes and tend to have higher fractal dimension than in surrounding normal regions. Findings are promising since they can be integrated into any framework for breast cancer detection and diagnosis.

ACKNOWLEDGMENTS

I wish to express my sincere thanks to Professor Ikhlas Abdel-Qader for her guidance and support. This research would not have been completed without her care, patience, constructive ideas and suggestions.

I also want to express my thanks to other members of my committee, Professor Liang Dong and Professor Dionysios I. Kountanis for their support.

Finally, I would like to thank my family for their unconditional support and love. They inspired me and gave me the strength to finish this work.

Tomislav Bujanovic

TABLE OF CONTENTS

CHAPTER

CHAPTER

Table of Contents—continued

LIST OF TABLES

LIST OF FIGURES

List of Figures—continued

CHAPTER I

INTRODUCTION

Cancer is a disease that causes cells in the body to change and grow out of control. There are many of the known relative breast cancer risk factors, such as age, family history, age at first full-term pregnancy, early menarche, late menopause, and breast density, postmenopausal obesity, use of post-menopausal hormones, alcohol consumption, and physical inactivity, but dominant cause is still unknown [1].

Excluding skin cancers, breast cancer accounts for more than 25% cancers diagnosed in US women. Unlike lung cancer, science does not know any significant prevention methods for breast cancer. On the other hand, it is a slow developing cancer and in most cases it needs 5 to 15 years to become palpable.

The earlier the breast cancer is diagnosed the higher chance is to be curable [2]. Early detection and diagnosis is the most important for the surgical cure while the disease is still bounded. From 1990-2004 death rates decreased by 3.3% per year among women younger than 50 and by 2.0% per year among women 50 and older [3]. The decline in breast cancer mortality since 1990 has been attributed to both improvements in breast cancer treatment and to early detection related to screening mammography [4].

Men are generally at low risk for developing breast cancer, accounting for approximately 1% of breast cancer cases in the US. Since mammography is recommended for women only, men are more likely than women to be diagnosed with advanced disease and have poorer survival [5].

The goal of numerous researcher efforts is to develop the tools for early detection of breast cancer.

Breast and Breast Abnormalities

The breast is mammary gland made up of lobules, glands for milk production, and the ducts that connect lobules to the nipple. The remainder of the breast is made up of fatty, connective, and lymphatic tissue surrounded by skin. The breast is separated from the chest wall pectoral muscles by connective tissue. The glandular tissue consists of 15-16 lobes, with varying numbers of ducts and lobules, arranged radially from the nipple. The skin forms a smooth convex surface, surrounding the parenchyma, and separated from it by a layer of fat.

Breast can vary greatly in form, size and composition. The breast converges toward the nipple, and is generally symmetrical in shape.

Breast is dominantly of three basic compositions: fatty, fatty/glandular and dense. Some breasts are being comprised primarily of fat, while the others are glandular with variable amounts of fatty tissue. In some breasts the fibro-glandular region appears as an island-like density, while in the others it appears as a sparse assemblage of tissue. The composition of the breast may also change over time.

There is no a precise qualitative and quantitative definition of normal mammogram although it is possible to describe normal and undisturbed patterns.

There are a number of abnormal signs, which allow a suspected breast cancer to be detected, including masses, microcalcifications, asymmetric densities, and architectural distortion.

Breast cancer begins in breast tissue eventually forming mass. A mass is defined as a three-dimensional dense region with margins distinguishing it from the

surrounding parenchyma. Masses are classified by location, density, size, shape (round, ovoid, lobulated), and margins (circumscribed, ill-defined, stellate, or spiculated). Some masses are benign. They do not grow uncontrollably and they are not life-threatening. Breast cancer usually appears with disturbed ductal patterns. Some breast cancers are called in situ because they are confined within the ducts or lobules of the breast and can be cured. Moreover lobular carcinoma in situ, known as lobular neoplasia, is not a true cancer because it doesn't develop into cancer but it is an indicator of increased risk for developing invasive cancer in the future. Most cancerous breast tumors are invasive starting in the lobules or ducts of the breast and breaking through the duct or glandular walls invade the surrounding tissue of the breast. The seriousness of invasive breast cancer is strongly influenced by the stage of the disease when it is first diagnosed.

Microcalcifications are tiny granule-like deposits of calcium frequently associated with malignant or benign findings. They appear as bright spots in mammograms. Shape, morphology, and spatial distribution of individual microcalcifications are some of the features detectable in X-ray mammograms that suggest benign or malignant breast disease. Researchers have made few breast tissue classifications and have recognized more than twenty of those conventional features [6]-[8]. They have varying characteristics, regular in size and shape or heterogeneous, fine or coarse, smooth or jagged. They may be punctate, branching, linear, spherical, cylindrical. One acceptable simplification is to describe microcalcifications as ellipsoids of diameters between 0.05 mm and 1 mm. For early cancer detection, calcifications with spatial extent less than 0.5 mm are most important for clinical diagnosis. Particularly, this corresponds to calcifications in the order of roughly 0.1 mm in

diameter. Also, it agreed on that microcalcifications appearing in clusters may suggest malignancy while individual occurrences are of low clinical significance [9].

Breast asymmetry exhibits as breast tissue that is greater in volume or denser in one breast than the other.

The structures of the breast tissue converge toward the nipple. The disturbance in this symmetrical flow is called architectural distortion.

Breast Imaging Modalities

Numerous randomized trials and population-based screening evaluations have clearly shown that involvement of breast imaging technologies greatly improve breast cancer survival [10]. Treatment is more successful when cancer is discovered early, several years before physical symptoms develop.

X-ray mammography is highly sensitive, but often nonspecific whether or not a suspicious region is benign or malignant. The limitations of X-ray mammograms are that the 3-D compressed structures of the breast are projected into a 2-D image.

In many cases breast abnormal masses can be detected with magnetic resonance imaging that are not visible in X-ray mammography, particularly with the patients with silicon implants, with scars after breast surgery, and patients with mammographically dense breast tissue. Sensitivity of magnetic resonance imaging for breast cancer detection is often higher than that of X-ray mammography or ultrasonography separately [11]. One of the limitations of magnetic resonance is low specificity, which reduces the effectiveness in the differentiation of benign from malignant abnormalities, but the use of magnetic resonance images is to determine the stage of a disease, when the abnormality was already detected.

Ultrasound has been used as an adjunct to X-ray mammography in detecting breast cancer. Ultrasonography as a diagnostic modality has been documented on well differentiation of cyst vs. solid tissue appearance. The degree of probe pressure applied can cause anatomy to change shape, location, affect acoustic impedance or change the appearance of blood flow. The ultrasound energy can easily penetrate dense tissues, which are opaque and difficult to X-ray. In pregnant or lactating women or women with dense breast tissue or with radio-opaque breast implants ultrasound imaging modality can be a non-ionizing alternative to conventional X-ray mammography to detect microcalcifications.

Microwave (radar) system is not a tool for diagnosing breast cancer yet, but along with other screening tools may improve detection and limit false positive findings.

Further development of ultrasound, magnetic resonance imaging and computed tomography combined with X-ray mammography may lead to a novel effective system for breast cancer control. If an X-ray mammogram was found positive it might be followed by a ultrasound or magnetic resonance examination to reduce the number of unnecessary invasive biopsies.

In following section I will shortly discuss each of imaging modalities.

X-ray Mammography

X-ray mammography is the primary imaging modality used in the early detection of breast cancer. X-ray mammograms are typically obtained by applying compression to the breast using two plates parallel to the image plane. Mammography is a low dose X-ray procedure that allows visualization of the internal structure of the

breast. Today's modern screen-film units result in higher quality images with considerably lower X-ray dose than the general-purpose X-ray equipment used in the past. The application of digital mammograms is still significantly more expensive, but they are more accurate, especially for women with dense breasts.

The 25-30 kV tube voltages are used to produce low energy X-rays in the range of 15 to 25 keV, considered optimal in terms of relative attenuation of X-rays in breast tissue. Higher energy levels of X-rays decrease the attenuation losing the mammogram details. The X-ray photons are transduced by a rare-earth screen into visible photons on the photographic film in contact with the screen. Superimposition of the densities from hundreds or thousands of about 1 mm diameter breast lobules and the ductal structures result an X-ray image, unlike most other X-ray or computed tomography images has an inherent fuzzy or diffuse appearance. A mammogram is composed of radiolucent or dark areas associated with fat, soft-tissue densities in various grayscale intensities, and radiodense bright area associated with calcium in calcifications or with other abnormal tissue growth.

Like most medical tests mammography is not perfect. Toady's mammography is very accurate detecting about $80-90\,\%$ of breast cancers in women without symptoms. Testing is more accurate in postmenopausal than in premenopausal women [12]. Despite advances in mammographic techniques, there are few shortcomings. The first of these limitations is the inherent 2-D nature of mammograms. This results in both the consolidation of the 3D structures of the breast into a 2-D projection image and the deformation of internal structures during compression.

The standard mammographic screening may yield four images; the medio-lateral-oblique and cranio-caudal view of each of the left and right breast. In a medio-lateral-oblique projection, compression is applied sidewise from the centre of

the chest wall toward the outer surface of the breast. In the cranio-caudal projection, compression is applied from the top of the breast toward the caudal surface [13].

The medio-lateral-oblique projection is considered the most useful view since it allows the greatest amount of breast tissue to be visualized. The cranio-caudal view offers additional information, improving the understanding of the three-dimensional structure of the breast. Usually the patients who undergo biopsy have diagnostic mammograms that include special views, other than medio-lateral-oblique and cranio-caudal projection.

Mammograms are often interpreted by analyzing a pair of corresponding views of each of the left and right breasts, and, when available, examining the same view of the same breast from previous studies. Temporal analysis relates to the comparison of corresponding mammograms of the same patient taken at different times, while bilateral analysis relates to the comparison of the left and right breast images within the same study. A deviation from the symmetry can be a signal of the presence of an abnormality. Masses appearing brighter than surrounding tissue are the most important asymmetric indication of a potentially suspicious region. Another indication of an abnormality may be a disturbance in the normally symmetrical flow of structures toward the nipple [14]-[15].

In conventional screen-film system small emulsion continuity faults may exist on the X-ray mammogram films, looking like microcalcifications [16]. These artifacts are usually sharply defined and brighter than the microcalcifications, and the size of the artifacts is within 3×3 pixels in most experiments.

Full field digital mammography is an imaging technology with flat panel digital detector with the capability to acquire and processes images in near-real time. It provides a quick check of positioning and possible motion blur. The system eliminates

photocell placement identifying the densest portion of the breast. This enables the technologist to focus on the patient rather than the system [17].

The newest digital full-field mammography systems use phase contrast imaging. The X-ray attenuates after passing through the object due to photoelectric effect and Compton scattering changing its amplitude. At the same time, after the penetration of the X-ray through the object, an X-ray shifts its phase in addition to the amplitude change. The phase shift is observed generally as refraction and interference. The interference takes place in only with coherent waves [18]. Detection of the phase shift as a difference in X-ray intensity is defined as phase imaging, while the difference in image density due to the phase shift is defined as phase contrast.

In the image quality of a phantom, the phase contrast mammography exceeded the screen film system. In the case of both mass and microcalcification, the ROC analysis A_z values of the phase contrast mammography clinical images overpass the screen film images. Clinical trials suggest superior detection of both mass and microcalcification by full-field digital phase contrast mammography over conventional SF mammography [19]-[20].

Magnetic Resonance Imaging of the Breast

Magnetic resonance imaging uses magnetic field to align nuclear magnetization of particularly hydrogen atoms in water, i.e. radiofrequency waves are used to extract image information from the human body through the interaction of these waves with the magnetic properties of atomic nuclei, according to their varying density and chemical binding in the tissues [21].

Sensitivity of magnetic resonance imaging for breast cancer detection is often higher than that of X-ray mammography or ultrasonography. One of the limitations of magnetic resonance is low specificity, which reduces the effectiveness in the differentiation of benign from malignant abnormalities [11]. Once the presence of a malignancy has been confirmed, the use of magnetic resonance images is to determine the stage of a disease or how far it has progressed. Factors used in determining the stage are the number, size, and shape of tumors. In many cases suspicious entity that are not visible in X-ray mammography, can be detected with magnetic resonance imaging. A mammogram that is positive may be followed by a magnetic resonance examination to reduce the number of unnecessary invasive biopsies.

Contrast-enhanced magnetic resonance imaging of the breast was first introduced in 1986 [22]. A contrast-enhanced magnetic resonance study of the breast is acquired as a sequence of 3-D images, before and after the administration of a paramagnetic contrast agent. A contrast agent is a pharmaceutical which changes signal intensity of one tissue relative to another and thus increases the tissue information content of an image [23]. The first image, referred to as the pre-contrast image, is acquired prior to the introduction of the contrast agent. The contrast agent is preferentially deposited into certain tissues changing the signal intensity of the tissues in the post-contrast magnetic resonance image. The contrast-enhanced magnetic resonance imaging takes post-contrast images at some time intervals depending on the interaction of the contrast agent and studied tissue.

Magnetic resonance images allow the time visualization of the contrast agent as it passes through the breast. Malignant abnormalities exhibit early rapid enhancement, followed by a period of slower enhancement. Benign abnormalities, on the other hand, tend to show a slow rate of enhancement [24].

In a magnetic resonance image, glandular and connective tissue has low signal intensity, while fat is visualized with moderate signal intensity. The contrast agent does not normally enhance glandular, fatty and connective tissue i.e. these structures do not change their appearance in pre-contrast and post-contrast images. Potentially suspicious regions as well as vascular structures can be traced through the images as enhanced structures of high signal intensity. For example, the pre-contrast image, the cyst appears as a bright region, while in the post-contrast image the cyst appears as a darker region. Particularly, a cyst and an enhancing mass are set to behave exactly opposite in signal intensity on the pre-contrast and post-contrast images. The change can be evaluated by comparing the pre-contrast magnetic resonance image with the corresponding post-contrast magnetic resonance images in a manner of comparing temporal mammograms.

The 3-D MR images could be visualized by few different approaches: volume rendering, volume slicing and surface rendering [25]. Isosurface rendering is an extraction of an intermediate surface description of the relevant structures from the 3-D information. In volume slicing, a 3-D image is presented as a series of 2-D slices which represent sections through the volume, normally taken in all three spatial dimensions. A maximum intensity projection is a form of surface-rendering, and is commonly used in the visualization of vasculature. The intensity changes in the tumor, associated vasculature and the cyst are easily observed.

Ultrasound Breast Imaging

Ultrasound based diagnostic medical imaging uses the frequencies above human hearing of 20 kHz. Typical operating frequencies are 2 to 18 MHz, where

higher frequencies are used more for breast imaging because of better image resolution in that range. Ultrasound is very efficient in making difference between cyst and solid but does not allow differentiation of a malignant from a benign appearance [26]-[27].

Probe pressure is critical in the evaluation of superficial anatomy. Light probe pressure applied over a suspected breast lesion may result in shadowing, indicating malignancy. Varying probe and graduated pressure flattens the tissue and the posterior shadowing is diminished or completely disappears, reducing suspicion for malignancy.

Ultrasound has been used as in addition to X-ray mammography in detecting breast cancer, because in the detection of microcalcifications the resulting sensitivity of ultrasound is low comparing with mammograms [28]-[29].

The breast is composed primarily of soft tissue and it deforms substantially during the ultrasound scanning procedure. Application of three-dimensional ultrasound imaging has better disease assessment capabilities than conventional two-dimensional imaging of the breast. Using a block matching scheme and local statistics to estimate local tissue deformation, Xiao et al. developed fully automatic algorithm for 3-D nonlinear registration of free-hand ultrasound data [30].

Spiculation is a stellate distortion caused by the intrusion of breast cancer into surrounding tissue. 2-D ultrasound cannot easily find spiculations because they normally appear parallel to the surface of the skin. In [31] the tumors found by the physicians are analyzed from 3-D ultrasonic volume data. Huang et al. proposed algorithm estimates the direction of the edge of each pixel around the central region. A pixel whose edge points toward the central region is marked as a potential spiculation.

Mammography Using Microwave

Mammography using microwave is not a tool for diagnosing breast cancer yet, but the studies show its ability in enhancing the results. Radar systems used along with other screening tools may improve detection and limit false positive findings.

Radar reflections depend on other materials and it can be used to detect diseased tissue, because of the difference between dielectric properties of diseased and regular breast tissue at very high frequencies.

Tissue sensing adaptive radar sends an extremely short pulse to the breast at each scan position and observes the reflected signal. The presence of an abnormality could be detected by analyzing the signal reflection by the sophisticatedly developed algorithms.

Radar systems avoid X-ray radiation and breast compression in mammography. They have potential of detecting very small cancer. Power of radar pulse is low as well as that of cell phone.

The fact that breast tumor exhibits electrical properties different from those of healthy breast tissues supports using to microwaves in breast imaging. Two approaches of active microwave imaging are applicable: analysis of reflected signal (confocal technique) and analysis of scattered signal (microwave tomographic technique).

Fear et al. described initial experimental verification of confocal microwave imaging for breast tumor detection using simple phantoms, consisting of a poly-vinyl-chloride pipe and objects representing tumors. They employed resistively loaded monopole or horn antennas to demonstrate reduction of clutter and detection of a variety of two-dimensional objects [32].

Shorter wavelengths improve spatial resolution, but at the cost of increased propagation loss in analysis of bio-systems. Similarly to ultrasound, a suitable coupling medium may improve the spatial resolution and provide less attenuation. Bindu et al. studied propagation loss of the medium and the radiation characteristics of the antenna in corn syrup as a coupling medium in microwave breast imaging. They reported improved resolution dealing with two-dimensional microwave tomographic imaging of a breast tissue sample immersed in corn syrup [33]. In the addition breast permittivity profiles are obtained in [34] based on variation of dielectric permittivity in breast samples.

The heterogeneous target zone within the antenna array can be modeled using the finite-element method, while the surrounding coupling medium is homogeneous and should be modeled with the boundary-element, which is important feature of a Gauss-Newton iterative scheme for microwave breast image reconstruction. The interface between these two zones may be arbitrary in shape and position with the restriction that the boundary-element region contains only the homogeneous coupling liquid. Li et al. demonstrated that the detection of tumor inclusions could be enhanced as the target zone approaches the exact breast perimeter and showed that central artifacts that appear in the reconstructed images is potentially reduced ability to distinguish benign and malignant tumor [35].

Early Detection in Breast Cancer Screening Procedure

In this work I discuss mammography as high resolution X-ray imaging of the compressed breast by projection of 3-D anatomical information to a 2-D screen. Although often nonspecific in terms of benign versus malignant, high spatial resolution of X-ray mammogram and adequate contrast separation allows radiologists to observe

fine structures in breast tissue. Reading mammograms requires excellent experience, but studies show high rate up to 30% of breast cancer fails to be detected at screening not only because of human eye limits and radiologists fatigue but also the complex image structure of the breast and the subtlety of the cancer [36]. False positive reading rate of negative or benign noncancerous mammograms may vary up to 15.9% [37] putting the patients emotionally to survive cancer.

If cancer is detected a woman is usually required to undergo further testing which may include an ultrasound scan of the breast, fine core needle aspiration, core biopsy, and diagnostic open biopsy – a surgical biopsy performed with a needle localization technique.

Overview of the Dissertation

The detection of microcalcifications can be easy over fatty background but challenging over dense parenchyma. The goal of numerous researcher efforts is to develop the tools for early detection of breast cancer.

Magnetic resonance imaging is high sensitive method that produces many false positive readings. Ultrasonography has high ability to make difference between malignant and benign masses, but its low sensitivity can cause false negative reading. Both methods magnetic resonance imaging and ultrasound has been used as an addition to X-ray mammography in detecting breast cancer. The goal of this work is to develop a method that is able to detect more suspicious regions in X-ray mammograms and let the radiologist to, focusing on those regions, make the decision.

In this work I propose a novel highly sensitive method for detection microcalcification that is not dependent on background tissue characteristics. I use

detected singularities, modeled as smoothed impulse functions, as seed points to perform microcalcification segmentation process.

Background on the detection and diagnosis methods, continuous wavelet transform, modulus maxima method, and fractal dimensions and their applications in mammography are presented in Chapter II.

In Chapter III I present the details of the proposed framework of microcalcification localization using general modulus maxima while in Chapter IV the performance of the proposed method is analyzed on a set of 25 microcalcification clusters. In Chapter V I show how to detect microcalcification cluster and employ local intensity maximum of underlying mammogram to reduce false positive and false negative findings along with a segmentation algorithm based on localized microcalcification and its initial edge detection to demonstrate efficiency of the method in breast cancer early detection. Conclusions and future work are presented in Chapter VI.

CHAPTER II

BACKGROUND

Reading mammograms requires extensive experience and up to 30% of breast cancer fails to be detected at screening by radiologists [36]. Disease diagnosis depends on radiologist's limitations related to mammogram interpretation due to the nonsystematic search patterns of humans, the presence of structure noise in the image, and the presentation of complex disease states requiring the integration of vast amounts of image data and clinical information [38]. It is also well known that human eye is not able to make difference if a region differs from its surroundings by less than 2% in luminance [39].

An early sign of 30–50% of breast cancer detected mammographically is the appearance of microcalcification clusters, i.e. upon histological examination 60–80% of breast carcinomas reveal microcalcifications [40]. The fact that microcalcifications appear in mammograms as spots in the range from 50 μm to 1 mm brighter than their surroundings enabled development of many computer aided methods for early detection and diagnosis. For examples, the computer aided methods have been able to increase microcalcification detection Receiver Operating Characteristic (ROC) area index $A_z = 0.92$ [41] or microcalcification diagnosis sensitivity (true positive fraction) up to 100 % for a false positive fraction of 85 % with receiver operating characteristic area index $Az = 0.98$ [8], for tested data set.

Standard procedure of a medical detection method evaluation using ROC curve and area index A_z is illustrated on Fig. 2.1.

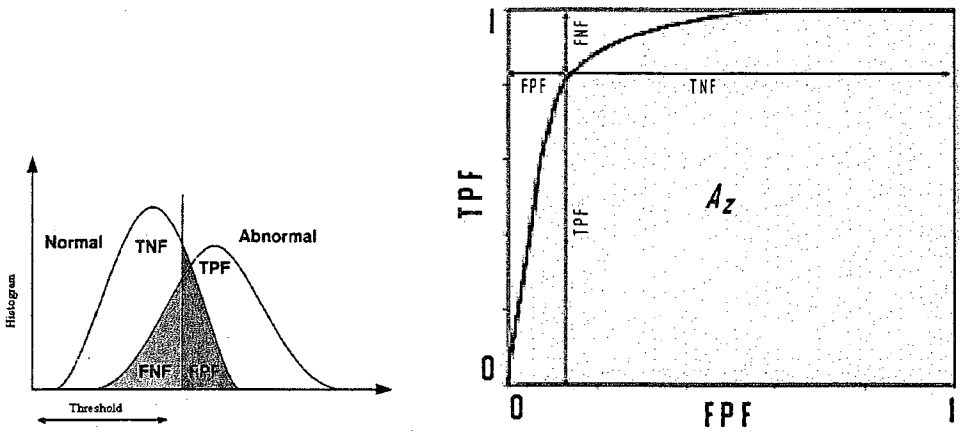

Figure 2.1. A threshold value yields the true positive, false positive, true negative and false negative findings from the distribution of the normal and abnormal targets – Fig. 2.1 (a). Changing the threshold ROC curve is defined as TPF vs. FPF. True positive fraction (TPF=sensitivity) is the number of abnormal targets classified as abnormal over total abnormal. True negative fraction (TNF=specificity) is the number of normal targets classified as normal over total normal. False positive fraction (FPF=1-specificity) is the number of normal targets classified as abnormal over total normal. False negative fraction (FNF=1-sensitivity) is the number of abnormal targets classified as normal over total abnormal.

R2 Technology Inc., Hewlett Packard Co., Sterling Diagnostic Imaging, Siemens, GE, and MedDetect/Lockheed Martin are the commercial companies that have developed and designed mammography systems for clinical applications. ImageChecker (R2 Technology Inc.) is a commercial algorithm approved by the US Food and Drug Administration (1998), by the Japanese Ministry of Health and Welfare (2000) by CE Mark certification in European Union (2000).

The performance obtained on a large set of cancer cases accomplished 98% sensitivity with a false-positive rate of 0.3 clusters per image [42].

Because five year survival rate is significantly higher if breast cancer was discovered early [2], the goal of numerous researcher efforts is to develop the tools for

early detection of breast cancer and particularly the presence of microcalcifications as an important sign for the detection of early breast carcinoma.

The directions for future research are designing better algorithms for enhancement, segmentation, feature detection, and target selection, improving classifiers that reduce both false positive and false negative results, standardizing test sets - databases, and standardizing evaluation criterions. Also, new work in computer-aided detection of abnormalities in mammograms should address evaluation issues properly since investigators need to know if and why new proposed methods really are improving existing ones. The use of phase-contrast imaging techniques [19], [43] may improve the contrast of radiographs and lead to enhanced imaging of the soft-tissue of the breast.

In this work I will focus on wavelet transform modulus maxima method because of its high sensitivity to detect and localize signal singularities and supported by fractal theory to classify them.

In the following five subsections I present a review of existing computer-aided methods of microcalcification detection and diagnosis, as well as some of the necessary background material on wavelet transform modulus maxima method and fractals, and their application in mammography.

Computer Aided Detection and Diagnosis of Microcalcifications

There are many computer aided systems developed for automated detection and classification of microcalcifications. In this sub-section, I review the algorithms used for the computer-aided mammographic feature detection, enhancement and segmentation, and classification.

One of the reasons for employing automated computer-aided analysis techniques in the interpretation of mammograms is the inability of the human vision system to distinguish more than 30 shades of gray [44], while a standard 12-bit mammogram contains $2^{12} = 4096$ shades of gray.

Computerized detection involves isolation of the breast region of the mammogram, identification of regions containing possible disease signs, and analysis of the features within these suspicious regions [45]-[46].

There are two general approaches explored in the detection of potential abnormalities in mammograms: single-image analysis, which analyzes a single mammogram for evidence of suspicious regions, and comparative analysis, which compares various corresponding mammograms.

In first step, the regions of interests selected from the digitized mammogram should be appropriately de-noised and enhanced for better performance. In second step, the segmentation is designed to find suspicious areas containing microcalcification clusters, and to separate them from the background. In third step, the features of microcalcifications are selected and extracted. In fourth step, microcalcifications are classified into benign, malignant or normal [40].

Enhancement of Microcalcifications

Image enhancement is performed by employing image processing techniques that have high contrast output protecting and/or enhancing previously defined significant signal features on one side or/and suppressing signal feature that are irrelevant or disturbing for the image analysis on another side.

Indirect contrast enhancement modifies the histograms without defining the contrast, while direct approach first defines the contrast and then enhance the contrast based on the defined measurements. Contrast enhancement algorithms can use global information. If the significant features have local variation contrast enhancement algorithms can use local or both global and local information. The enhancement image techniques are more efficient when input signal and desired and/or suppressed features are well known. If it is not the case, the contrast enhancement algorithms can under or over enhance different regions of an image, causing false negative and false positive classification decisions.

Image enhancement methods applicable in mammography can be categorized as conventional (contrast stretching, histogram equalization, convolution mask enhancement, fixed and adaptive pixel neighborhood enhancement), region-based enhancement, and microcalcification feature-based enhancement. Conventional enhancement methods often enhance or suppress both significant and irrelevant features in mammograms because of their high level of randomness [47]-[49].

Region based methods can enhance more anatomical details and can be more effective with dense breast where the contrast between microcalcification and the tissue is low [50]. Contrast is enhanced by empirically formulated transformation based on seed pixel value, contrast and background of each region. Feature based enhancement is performed by image sub-band decomposition and then higher order statistics (skewness, kurtosis) is calculated in the bandpass subimages [51]-[52]. This technique assumes that the analyzed region has normal (Gaussian) distribution if value of skewness and kurtosis is close to zero implying no microcalcifications were present. Similarly, fuzzy set theory was used to increase contrast of microcalcifications since mammograms have some degree of fuzziness as indistinct borders, ill-defined shapes,

and different densities [53]. Microcalcifications were enhanced by using high frequency subimage if healthy breast tissue is considered as smooth low frequency background [54]. Fractal approach could be used to model breast tissue background that differs from microcalcification if high local self-similarity of healthy tissue is considered as the pattern [55]

The fractal and morphological approaches showed higher efficiency in background healthy tissue structures removal, but multiresolution approach were able to preserve the shapes of image details better than fractals.

Segmentation of Microcalcifications

Segmentation is a procedure that divides an image into non-overlapping regions. The goal of segmentation is that by defining the suspicious areas in mammograms to assist radiologists to classify the abnormalities in benign or malignant.

Some segmentation techniques use global and/or local statistics (statistical and Markov random field based methods), others group pixels in homogenous groups (region-based method), thirds use morphological filters to extract the edges and to threshold the region (mathematical morphology), fourths use subband images for further processing (multiscale analysis), fives use local self-similarity to model fractal objects (fractal model analysis), and some techniques use fuzzy rules which is appropriate due to variable shapes of microcalcifications, but difficult for fuzzy membership definition.

Statistical methods use global or local statistics such as histogram, mean, standard deviation, just to name a few. There is no need for a priori information for the histogram thresholding of the image. They work very well with low computation

complexity, but they are parameter dependent and do not work without peaks [56]-[59].

Region-based approach groups pixels into homogeneous regions. It works well if there exist the region homogeneity criteria easy to define. It depends on the selection of seed region and the termination conditions. Region growing approach needs a previously determined seed pixel and groups the neighborhood pixels using similarity metrics to the seed pixel. If the average intensity of the grown region is greater than the surrounding region, the pixel is classified to belong to the microcalcification. The procedure is repeated while every pixel in the image is classified [60]-[61].

Mathematical morphology is a method that extracts the edges or skeleton information using morphological filters. The results are not affected by the complex background. It is efficient with geometric analytic aspects of image analysis problems. It is able to adapt to the sizes and shapes of the structure elements in multiscale and multi-structuring analysis if a priori knowledge of the resolution level of the mammograms is available. Edge detection using Sobel gradient, Prewitt gradient and Laplacian operator is a traditional method for segmentation. Erosion, top-hat transformation and more complicated morphological filters with multi-structure elements are applicable mathematical morphological operation [62].

Multiscale analysis is a wavelet-based transform of the image from spatial domain to spatial-frequency domain, preparing for further processing. The method does not require the use of a prior knowledge of the size and the resolution of the mammogram. The cancerous mass will be visible in lower frequency subimage while finer microcalcifications will be detected in a high frequency level. Using wavelet transform, the detection of microcalcification is a reconstruction of the image from transform coefficients modified at each level by local and global nonlinear operators.

The wavelet transform could separate small objects (microcalcifications) from large objects (background structures) [63]-[65].

The fractal model uses the fact mammograms possess structures with high local self-similarity, which is the basic property of fractal object. General mammographic parenchymal and ductal patterns can be modeled by a set of parameters of affine transformations. Microcalcifications can be enhanced by taking the difference between the original image and the modeled image. This method is able to improve the detection and classification of microcalcifications in a computer-aided diagnosis system [66].

Fuzzy operators, property, and inference rules have high ability to handle the uncertainty inherent in the mammograms. Using fuzzy rules fuzzy approach perform approximate inference efficiently due to variable shapes of microcalcifications. The determination of fuzzy membership is usually very complex [67]-[68].

Microcalcification Detection

There are several microcalcification detection approaches based on feature extraction methods: template matching, individual microcalcification features, microcalcification detection based on statistical texture features, microcalcification detection based on multiscale texture features, microcalcification detection based on fractal dimension features, and microcalcification cluster detection using clustering features [40].

Individual microcalcification features originate from the experience of radiologists [69]-[72]. Based on the feature description (perimeter, area, compactness, elongation, eccentricity, thickness, orientation, direction, line, background,

foreground, distance, and contrast) they are easy to be extracted from mammogram directly.

Co-occurrence features are features extracted from spatial gray level dependence matrix (co-occurrence matrix) [73]-[75]. Surround region dependence features are four directional weighted sums: horizontal, vertical, diagonal, and grid [76]. A grey-level run is a set of consecutive and collinear pixel points having the same gray level value and its length is the number of pixel points in the run. Gray level difference is a set of five features that can be extracted from estimated probability density function. This method is based on the occurrence of two pixels having a given absolute difference in gray levels and separated by a specific displacement (contrast, angular second moment, entropy, mean, and inverse difference moment) [76]-[77].

Providing a powerful framework for multiresolution analysis, wavelet theory can be used for texture analysis [78]-[82]. A set of features related to a region of interest can be extracted from each scale of the wavelet transform. The features that reflect scale dependent properties are developed from wavelet coefficients. The most frequently used features are energy, entropy, and norm of the coefficients [69]-[70], [75]. For example, two wavelet transform coefficients and two local statistic features (median contrast and normalized gray level value) were capable to result 93% true positive and 1 false alarm per image on the tests of 40 images from Nijmegen database [69]. Same authors used same methodology when applied a set of 31 features. They reduced the false alarm rate to 0.5 per image, but the true positive detection rate also dropped to 90% [70].

Texture features extracted from co-occurrence matrix and wavelets as the inputs to a neural network resulted a maximum area index $A_z = 0.74$ under ROC curve

in detection of the microcalcifications in 191 hard to diagnose mammograms [83]. The area under ROC curve increased to $A_z = 0.86$ by adding more cluster features [75].

Scale-space features are features extracted from the image processed by Laplacian of Gaussian filter. By changing the size of the filter, this method transforms the original image into different scale spaces. The Laplacian of Gaussian response at different scales is calculated as the feature. The magnitude of Laplacian of Gaussian response of microcalcification was compared with a threshold to make decision if a spot is considered microcalcification or not [63].

Fractal dimension is a feature extracted from fractal model of the image. Image roughness can be measured by numerical value of its fractal dimension. Smoother and rougher areas of the images have different fractal dimension values. The fractal dimension or fractal capacity is the exponent D in $n(\varepsilon) = \varepsilon^{-D}$, where $n(\varepsilon)$ is the minimal number of balls of diameter ε needed to cover the fractal set in each scale and D is a constant characteristic of the surface. More discussion on fractal dimension will be presented in Section II.5.

Cluster features are features used to describe the distribution of the microcalcification, cluster area, and number of microcalcifications in an area. They include spatial features, morphology features, and the cluster description features and/or the distance between the microcalcifications as a measure to group microcalcifications into clusters. After individual microcalcifications are detected, cluster features are used to group them into clusters. The number of microcalcifications could be used within a region of a fixed area. Based on medical databases, a cluster is declared if there is at least three microcalcifications in 1 cm^2 square [84]-[87].

Malignancy Analysis

The feature sets are mostly the same with those used for microcalcification detection: wavelet features, co-occurrence features, surround region dependence features, individual microcalcification features, and cluster features.

Wavelet features are energy, entropy, and norm extracted from the wavelet decomposition of the original mammogram into its sub-images [83],[88].

Co-occurrence features can be metrics for image texture. They are being extracted from the gray level co-occurrence (spatial dependence) matrix [83], [88]-[91].

In surround region dependence method the features are four directional-weighted sums that represent directionality in a pixel-surrounding region [92].

Compactness, moments, average of the gray level are individual microcalcification features extracted directly from a mammogram [89]-[93].

Cluster area and number of microcalcifications in an area are cluster features used as the metrics for the distribution description of the local features in the detected clusters [90]-[91], [93].

Four different classifiers (neural networks, K-nearest neighbor, Bayesian classifier, and decision tree) employ the features or a subset of these features and classify microcalcifications into benign and malignant [40].

An artificial neural network (NN) is a parallel-distributed information processing structure consisting of artificial neurons functionally related by directional connections. An artificial neuron carries out local operations. The neural networks are used for solving artificial intelligence problems without necessarily creating a model of a real biological system. The neural networks are suitable for applications where an input-output complex nonlinear relation is not known in advance and needs to be

learned. They process a large input data making only a few decisions. Through examples contained in a training set, artificial neural networks may provide a better solution than expert systems. If the expert knowledge cannot be represented in terms of statistically independent rules or there is no explicit rule definition artificial neural networks can efficiently conduct complex decision making. Simultaneously artificial neural networks can learn how to find a new data pattern during the classification procedure. For example, a set of 10 surrounding gray level difference features extracted from 85 difficult-to-diagnose mammograms produced a classification accuracy of 74% [94]. The neural network were able classify correctly 89% of the 40 cases from Nijmegen database [93]. A simulated annealing optimization technique may improve the optimal neural network architecture [95]-[96] as well as genetic algorithms for differentiating malignant from benign [97]-[99].

K-nearest neighbor (KNN) algorithm classifies objects based on closest training examples in the feature space. This is one of the simplest learning methods which uses the similarity of the unknown patterns to known samples and computes the distances from an unknown pattern to every sample. K-nearest neighbor classifier selects the K nearest samples as the base for classification. The unknown pattern is assigned to the class by a majority of its neighbors containing the most samples among the K-nearest samples [100]-[101]. An experimental comparison of microcalcification classification performance showed higher classification accuracy of NN than KNN based classifiers [102].

Bayesian belief network (BBN) is an optimal pattern recognition method, which determines an optimal segmentation given a specific database using a probability value associated to each variable with at least two discrete states. The total of probability values for all states and for each node equals 1. The probabilistic

independence of two variables is indicated if there is no path between any two nodes belonging to the variables. Despite the early results showed that Bayesian classifiers may outperform artificial neural networks [103], the performance of the two techniques should converge to the same level. The performance of a CAD system should be dependent on feature selection and training database, but generally independent of any particular classifier.

Binary decision tree is a data structure used to represent a Boolean function. Each decision node is labeled by a Boolean variable and has two descendent nodes, differentiated by a threshold value of the feature. This procedure will continue until it arrives at a terminal node that assigns a classification. The threshold of a feature which best separate the current data into two classes sets the control parameters at each node. The process generates a tree by recursively partitioning the remaining training samples [104].

Comparing with neural networks, the decision tree approach is much simpler with low computational overhead. In addition it does not need extensive knowledge of the probability distribution of the features such as the case with Bayesian classifier.

In mammograms binary decision tree might not be efficient and fuzzy logic could be used to improve the performance of decision tree [105]-[107]. Using a grading membership the algorithm follows the alternative paths on both sides of the threshold of the test.

Pertinent Literature

There are many approaches how to improve computer analysis for the detection and diagnosis of breast cancer. Among the first uses of mathematical microscope in mammograms is Wang and Karayiannis [108] who proposed searching

for microcalcifications by using high frequency energy blobs in wavelet decomposed mammograms. They took advantage of the fast algorithm which is based on filter banks. In practice, only the dyadic wavelet transform is considered to take advantage of the fast algorithms implemented by filter banks. Also, high frequency energy blobs are not the sign of disease in mammograms by themselves and normal signal fluctuation in mammograms may have dominant energy blobs in some scales making a mask over significant disease related information. Indeed, an energy blob is just a location where further analysis should follow.

Zhang et al. [41] studied the size of microcalcifications and developed an optimally weighted wavelet transform method by which, before image reconstruction, they multiplied dyadic wavelet coefficients by 0.4, 1.6, 1.0, and 0.05 for the scales corresponding to 100 μm, 200 μm, 400 μm, and 800 μm respectively. This means that information related to second and third level of dyadic decomposition for the given resolution of 100 μm is the most significant for microcalcification detection. They achieved $A_z = 0.92$ under ROC curve, outperforming $A_z = 0.86$ for difference-image technique. Their results are based on the microcalcification size appearing in their database showing that the most common microcalcification diameter is in the order of 200 μm. This weighting coefficients method has shown a lower recognition capability for the targets smaller than 200 μm and bigger than 800 μm. Their weighting coefficients should be adjusted to spatial resolution of other databases.

Wavelet transform modulus maxima method was developed for detection and characterization of signal singularities by Mallat and his collaborators [109]-[111] in 1992. Their method detects signal singularities by tracking the wavelet coefficients magnitude maximum across the scales. They proved that, if a wavelet function is derivative of a Gaussian, wavelet transform modulus maxima must propagate towards

finer scales. Although the representation by discrete wavelet maxima is not complete since several signals may exhibit the same wavelet maxima [112], Mallat's numerical experiments have shown that it is possible to reconstruct signals with a relatively small mean square error (smaller than 10^{-2}) [111].

Bruce and Adhami [113] introduced three new multiresolution features related to the detected singular points in suspicious areas that quantify the mass shapes. They proposed using Gaussian filters in modulus maxima method with dyadic wavelet transformation and an optimization procedure to calculate Holder exponent, magnitude and standard deviation of smoothed impulse function. Comparing with traditional uniresolutional shape features, they were able to improve discrimination shape classes. Their method used dyadic wavelet transform by which they were able to detect normal signal fluctuation in mammograms. However, they were not able to sense sharp signal transition that often appears and disappears in less than one octave. Their diagnostic conclusions were based on non-differentiated normal signal fluctuation and sharp signal transition.

Tang et al. proposed a modulus maxima based method to detect and analyze Dirac-structure edges and reached to the conclusion that the edges are slope invariant, grey-level invariant, and width light dependent [114] which may prove to be useful in spiculated mass analysis or boundary analysis.

The regularity of a wavelet basis is also used to improve identification of clustered microcalcification in its early phases. Lemaur et al.[115] work pointed to the advantages of highly regular wavelets in the detection of microcalcifications in mammograms over Daubechies' [116]. They designed highly Sobolev regular wavelets with the purpose of detection of sophisticated signal singularities. They experimentally compared new wavelets' performance to the "classic" Daubechies wavelets' obtaining

larger wavelet coefficients modulus in true positive and smaller in false positive detection.

Scale-space theory is a framework for handling image structures at different scales [117]. In scale-space theory convolution with Gaussian kernels and their derivatives is regarded as a canonical class of low-level operators, i.e. the first stage of image processing should be as uncommitted as possible, with no particular bias.

Medical studies have shown there are many biological processes that can be successfully modeled by linear Gaussian derivative operators or their non-linear combinations [118] and [119].

Similarly, microcalcifications in mammogram analysis may be modeled as an impulse function smoothed by a Gaussian filter. Strickland and Hahn [120] recognized Gaussian nature of microcalcifications spatial intensity and applied 2-D Gaussian filters for microcalcification detection. They inserted inter-scales to increase detection sensitivity for wide range of possible microcalcifications.

A significant problem for a feature detection method expressed within a multi-scale framework has been how to determine at what scale an image feature has to be extracted or if the feature detection is performed at several scales what image feature has to be considered as significant. Significant features of microcalcifications may be fast changing over scale and coarse scale increment in the range of ½ or ¼ of an octave makes feature changes still invisible. Lindberg [121]-[122] developed a method for automatic scale detection in which a feature can be optimally recognized. He successfully applied the method for ridge and edge detection. Scale levels were selected at a certain blob measurement assumed local maxima over scales. Lindberg proposed a general heuristic principle stating that local maxima of the signal convolved

with combinations of normalized Gaussian derivatives over scales serve as a useful indicator that reflects the spatial extent of corresponding image structures.

Arneodo and his team [123]-[126] focused on how to recognize a sharp signal transition by tracking its behavior over scale. Specifically algorithms based on continuous wavelet transform modulus maxima method are able to detect singular points in a discrete 2-D signals and supported by fractal analysis to give the metrics for the local signal regularity. Arneodo's team developed fractal based algorithm [126] supported by modulus maxima method to analyze turbulent 2-D and 3-D signals. They showed that wavelet transform modulus maxima provides an adaptive space-scale partitioning from which they were able to extract the singularity spectrum via scaling exponents of some partition function defined on the skeleton of the modulus maxima. They described the methodology with some test applications to random monofractals and multifractal self-affine surfaces displaying isotropic or anisotropic scale similarity properties. They presented wavelet transform as a mathematical microscope that has been well suited for characterizing the local regularity of rough surfaces. 2-D wavelet transform modulus maxima method has been a natural generalization of box-counting algorithms and structure function techniques that had been used for multifractal analysis of isotropic self-similar interfaces and multiaffine surfaces. They showed that 2-D wavelet transform modulus maxima method could be used in image processing edge detection, pattern recognition, and image denoising.

In his doctoral dissertation [127] Pierre Kestener applied the algorithm developed by Arneodo et al. [126] to study the texture segmentation of rough surfaces and also he applied it to microcalcification detection in mammograms. Kestener used the algorithm to demonstrate its efficiency for breast texture classification. He showed that there are only two classes of fractal features, a dense one, which is characterized

by Hurst exponent of $H = 0.65$ having persistent correlation and a fatty one, characterized by $H = 0.30$ having anti-persistent correlation. He initially segmented the image using Holder exponent (or local roughness characterization) separating the areas with $h > 0.58$ for dense tissue and $h < 0.38$ for fatty tissue. Then, he constructed maxima skeleton and tracked modulus maxima in scale. Supervised classification of maxima lines pointing to microcalcifications can be based on growth of modulus maxima from higher to lower scale, existence of a specific transition scale in the border of the microcalcifications, and modulus maxima at lowest scales with magnitude characteristic for microcalcifications.

Using Marathon database (55 μm/pixel, 14 bits/pixel) and based on singularity spectrum, Kestener found that the detected slope $h \sim -0.4$ is pointing toward microcalcifications and asymptotic $h \sim -1$ has not been reached because of finite size effects (the maxima lines become overlapped by normal signal fluctuation in higher scales). He also concluded that the average microcalcification diameter is about 200 μm which is in agreement with results in [41] because their weighted coefficients are 1.6 for the scale corresponding to 200 μm and 1.0 or less for other dyadic scales. Also, he concluded that microcalcifications have typical sharp transitions $h \sim 0.0$ in scale 1.4 (corresponding to 70 to 80 μm) in which a microcalcification border is best visible, with detected slope $h \sim -0.4$ in the higher scales. He gave an example that fractal dimension for two malignant clusters are $D_F = 1.45$ and $D_F = 1.65$ in the same mammogram. For unsupervised classification Kestener suggested using neural networks or genetic algorithm based method to reinforce further microcalcification selection.

In this work, I propose to build on Lindberg's idea of feature extraction [121]-[122] to identify general modulus maximum and the scale in which it appears. I

also show that general modulus maximum is a significant tool for microcalcification detection. I identify the scale in which Holder exponent of smoothed impulse function approaches $h \sim 0.0$ and use detected magnitude as the most significant local information. I propose to achieve our goals by combining local spatial signal intensity with the scale of general maximum to improve microcalcification classification results.

Wavelet Transform and Localization of Isolated Structures in Images

The conjecture that Holder exponent of a strong singularity is negative has been confirmed in many experiments and successfully used in turbulent process modeling [128].

In mammograms the presence of strong local singularities is characterized by negative Holder exponent while normal fluctuation is characterized by positive Holder exponent. This makes an isolated singularity detectable by analyzing the behavior of a modulus maximum along its maxima line.

Mallat and Hwang [109] proved that the magnitudes of the wavelet coefficients are bounded as shown in (2.1):

$$\left|W_a f(x,y)\right| \leq A \cdot a^{\alpha} \tag{2.1}$$

where $\left|W_a f(x,y)\right|$ is magnitude of the wavelet coefficient at point (x, y) in scale a, α is Lipschitz (Holder) exponent at (x, y) and $A > 0$ is a constant [109].

When Holder exponent at (x, y) is positive the magnitude of wavelet coefficient will increase with scale while when it is negative, as in case of impulse function, the magnitude of the wavelet coefficient will decrease. In practice local microcalcification of the mammogram signal may be represented as impulse function convolved by a Gaussian smoothing function.

In general, suppose in the neighborhood of a sharp transition at a point u a smoothed function is defined by $f = f_0 * g_\sigma$ where f_0 is uniformly Lipschitz α on the interval $[u-\Delta x, u+\Delta x]$ and

$$g_\sigma = \frac{1}{\sigma\sqrt{2\pi}} \exp\left(-\frac{t^2}{2\sigma^2}\right) \tag{2.2}$$

where g_σ is Gaussian smoothing function with variance σ^2.

Convolving the function f by n^{th} derivative of a Gaussian filter with variance β^2 yields the wavelet coefficient that is bounded by

$$|Wf(u,s)| \le A a^{\alpha+\frac{1}{2}} \left(1+\frac{\sigma^2}{\beta^2 a^2}\right)^{-\frac{n-\alpha}{2}} \tag{2.3}$$

For further analysis of behavior of magnitude of wavelet coefficients in scale, a regression of (2.3) was performed yielding a wavelet coefficient magnitude approximation [111]

$$\log_2|Wf(u,s)| \approx \log_2(A) + \left(\alpha+\frac{1}{2}\right)\log_2 a - \frac{n-\alpha}{2}\log_2\left(1+\frac{\sigma^2}{\beta^2 a^2}\right) \tag{2.4}$$

If α tends to -1, then the wavelet coefficient increases up to a maximum of $\sigma = \left(\sqrt{2\sqrt{2}}\beta\right)\cdot a$, which is followed by a decrease [64], as shown in Fig. 2.2 and Fig. 2.3.

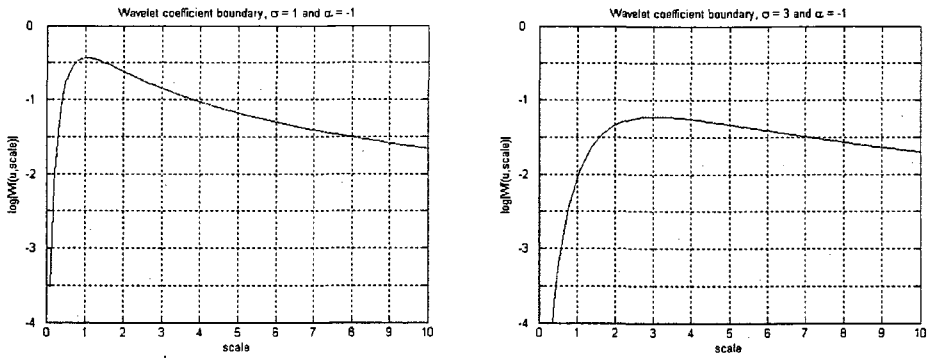

Figure 2.2. Illustration of expected bound for the evolution of modulus maximum along the scale for an impulse function of magnitude = 1 smoothed by Gaussian $\sigma = 1$ (left, maximum is at scale = 1) and $\sigma = 3$ (right, maximum is at scale = 3).

Modulus Maximum Representation

A Gaussian smoothing function

$$\phi(x,y) = \frac{1}{2\pi\sigma^2}\exp\left(-\frac{x^2+y^2}{2\sigma^2}\right) \tag{2.5}$$

has been used as a kernel for wavelet transform discrete filters. The horizontal and vertical wavelet coefficients at scale a are defined as

$$W_a^{hor}(f) = f * \psi_x \tag{2.6}$$

and

$$W_a^{ver}(f) = f * \psi_y \tag{2.7}$$

respectively, where the horizontal and vertical derivatives of smoothing function ϕ are defined by

$$\psi_x(x, y) = \frac{\partial \phi(x, y)}{\partial x} \tag{2.8}$$

and

$$\psi_y(x, y) = \frac{\partial \phi(x, y)}{\partial y} \tag{2.9}$$

respectively.

A wavelet coefficient at a scale ***a*** is represented by its magnitude and argument as follows,

$$W_a(f) = (M_a(f), A_a(f)) \tag{2.10}$$

where $M_a(f) = \sqrt{(W_a^{hor}(f))^2 + (W_a^{ver}(f))^2}$ and $A_a(f) = Arg(W_a^{hor}(f) + j \cdot W_a^{ver}(f))$, with horizontal and vertical wavelet coefficients $W_a^{hor}(f) = \langle f, \psi_x \rangle$ and $W_a^{ver}(f) = \langle f, \psi_y \rangle$ in scale ***a***, respectively.

A modulus maximum at (x_0, y_0) in scale ***a*** is represented by its magnitude if it is equal or greater than wavelet transform magnitude in its neighborhood. There is no detected modulus maximum at (x_0,y_0) in scale *a* if any surrounding wavelet transform magnitude is grater than magnitude at (x_0,y_0), i.e.

$$MM_a(x_0, y_0) = \begin{cases} M_a(x_0, y_0) & M_a(x_0, y_0) \geq \max\limits_{(x,y) \in \aleph(x_0, y_0)} M_a(x, y) \\ 0 & otherwise \end{cases} \tag{2.11}$$

where $\aleph(x_0, y_0)$ is 8-neighborhood of (x_0,y_0).

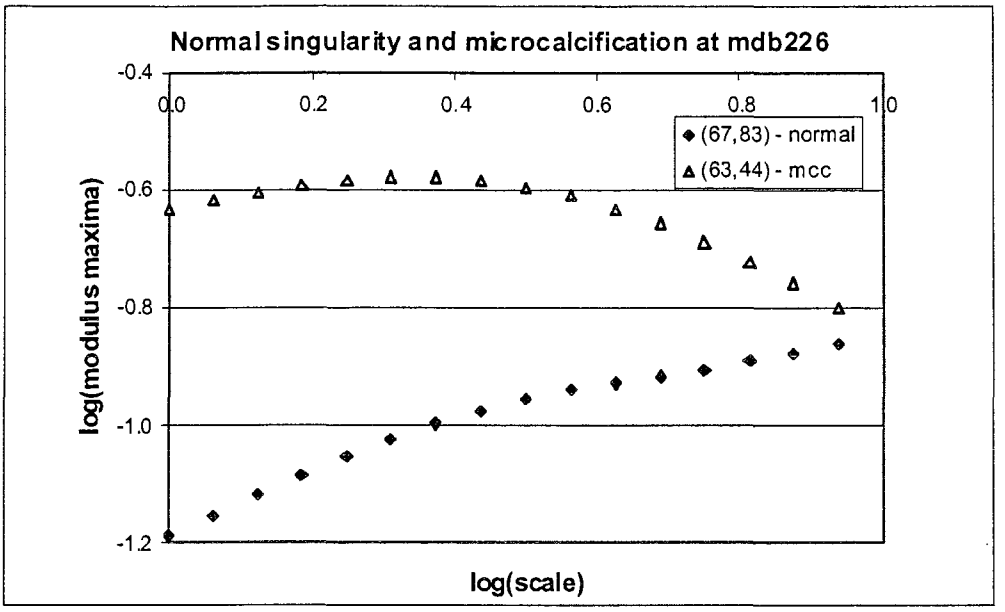

Figure 2.3. Typical log-log characteristics Modulus Maxima vs. scale for a normal signal fluctuation (♦) and a microcalcification (Δ) in mammogram mdb226 - MIAS database

While a maxima line consists of the wavelet transform modulus maxima corresponding to the same local feature but in different scales, the general modulus maximum is a point on the maxima line characterized by maximal magnitude gM and scale a_{gM} in which it is detected. Wavelet transform general modulus maximum will appear with a magnitude gM and in a scale a_{gM} that depends on the initial variance of the smoothing Gaussian in the initial scale $a_0 = 1$.

In the higher scales of a_{gM} corresponding maxima line will exist as long as the smoothed impulse function is the dominant singularity in its neighborhood. In that range the slope of the log-log diagram Modulus maxima vs. scale will tend to -1 if the maxima line is long enough, i.e. until it is overlapped by a modulus maximum of another dominant singularity. If in higher scales the singularity stops being dominant in

its neighborhood, the maxima line tracking process should be interrupted to prevent misleading singularity detection. The magnitude and the scale in which the general modulus maximum is detected as well as the length of maxima line afterward are significant starting points for evaluating the isolated singularities

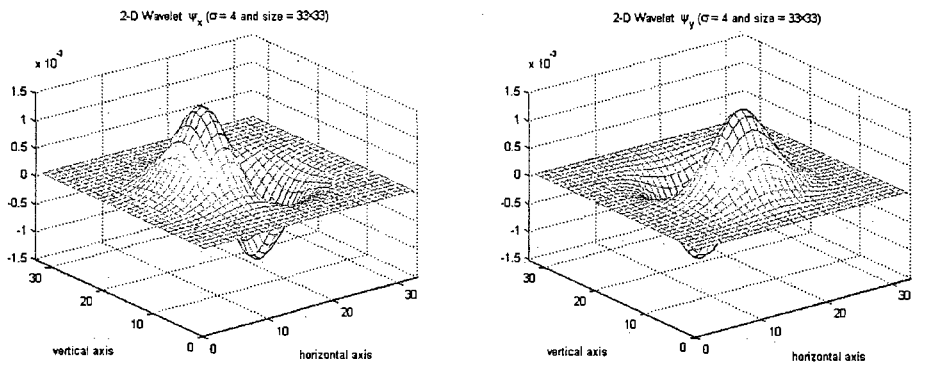

Figure 2.4. Horizontal and vertical 2-D wavelets ($\sigma = 4$ for 33×33 pixels)

Fractals, Partition Function and Fractal Dimension

A fractal is an object or quantity that displays self-similarity in all scales. A plot of the quantity on a log-log graph versus scale then gives a straight line, whose slope is said to be the fractal dimension. The prototypical example for a fractal is the length of a coastline measured with different length ruler. The shorter the ruler, the larger the length measured, a paradox known as the coastline paradox or 'the Richardson effect' (L.F. Richardson, 1881-1953) [129].

By definition fractal dimension or capacity dimension of a fractal is the exponent D in $n(\varepsilon) = \varepsilon^{-D}$, where $n(\varepsilon)$ is the minimal number of balls of diameter ε needed to cover the fractal set in each scale. Employing wavelets provides a natural generalization of the classical box-counting techniques to fractal signals, i.e. the

wavelets are playing the role of generalized boxes. The wavelet transform as a mathematical microscope can be used to extract microscopic information about scaling properties of fractal objects [126]. Partition function can be derived from maxima line skeleton as

$$Z(q,a)=\sum_{L\in\Lambda(a)}\left(\sup_{L,a'\le a}M_{\psi}\left[f((x,y),a')\right]\right)^{q},\ q\in\Re \tag{2.12}$$

The analogy related to multifractal formalism in thermodynamics allows the following definition of the exponent $\tau(q)$ for the behavior of partition function along the scale:

$$Z(q,a)\propto a^{\tau(q)},\ a\to 0^{+} \tag{2.13}$$

where q and $\tau(q)$ represent inverse temperature and free energy in statistical mechanics [126]. For homogenous fractal functions – monofractals and $q=0$, the value of $-\tau(q)$ is associated to fractal dimension of the set of all detected singularities [125].

Discussion

Existing methods for microcalcification detection are originated from standard image processing techniques. Some of very successful techniques in imaging can't reach satisfactory efficiency in mammogram analysis. For example, mammogram denoising should be delicately performed because noise and normal signal fluctuation in mammograms as well as microcalcifications are characterized by high frequencies in similar ranges. Also, there is no precise morphological description of microcalcification and morphological filters can enhance some targets but miss the others that do not fit to the filter specification. Statistical methods are efficient and

robust if the target appearance is statistically significant, which may not be the case in the early stage of the disease. Dyadic wavelet transform has been promisingly efficient detection tool, but some targets may be missed because their features were detectable in an inter-octave.

The singularity detection method proposed in this work is sensitive in the level of a single pixel lowering the need for additional breast screenings using MR or US medical imaging modalities.

Early detection using this method can be improved by focusing on investigation of behavior of microcalcifications detected in lowest scales.

I assume that a microcalcification may be characterized as a sharp signal transition detectable by wavelet transform as a mathematical microscope. I propose to build on Lindberg's idea of feature extraction [121]-[122] to identify general modulus maximum and the scale in which it appears. I take advantage of the capabilities of continuous wavelet transform modulus maxima method to detect signal singularities and differentiate microcalcifications and normal signal fluctuation using Holder exponent values. I accept consideration that microcalcifications are sharp signal transitions modeled as impulse functions smoothed by a Gaussian and characterized by negative Holder exponent. I detect smoothed impulse functions and select those with dominant magnitudes of general maxima.

I show that general modulus maximum is a significant tool for microcalcification detection. I identify the scale in which Holder exponent of smoothed impulse function approaches $h \sim 0.0$ and use detected magnitude as the most significant local information.

I focus on general modulus maxima because a selected smoothed function with dominant magnitude of its general maximum matches to the microcalcification nature.

Microcalcifications in mammograms appear as the spots brighter than their surroundings.

I propose to improve the detection performance by combining local spatial signal intensity with the scale of general maximum to improve microcalcification classification results

I employ local intensity maximum presence in the neighborhood of a selected singularity as a requirement for microcalcification detection to reduce false positive and false negative findings and hence to improve the detection method performance.

The general modulus maximum of a smoothed impulse function could be a complement to other features in existing detection algorithms to improve the algorithms' performance.

The method performance will be presented by analyzing 25 regions containing microcalcification clusters from diagnosed 20 mammograms and comparing the results to the results of 20 regions with healthy tissue from the same mammograms. Since general modulus maximum is a significant source of information about local signal behavior, I proceed with fractal dimension analysis of selected singularities in same regions. The algorithm recognizes microcalcification itself but not its transition border because of mammogram's coarse resolution used in this research. The scale of microcalcification detection depends on the size of the microcalcification since microcalcification size differs from one to another. The magnitude of a general maximum doesn't depend on the negative slope within the detection procedure. This makes general modulus maximum stronger and more independent feature i.e. that is an excellent candidate to integrate with other features.

CHAPTER III

SINGULARITY LOCALIZATION USING WAVELETS

In this chapter I will develop a method how to detect smoothed impulse function in a 2-D signal and show that general modulus maximum of smoothed impulse function is a significant feature for microcalcification detection in mammograms.

Singularity Selection and Microcalcification Localization

Normal signal fluctuation in mammograms can be recognized by positive Holder exponent at a point. A microcalcification in mammogram can be modeled as smoothed impulse function characterized by negative Holder exponent tending to -1.

Changing the scale, Gaussian filters are used to compute wavelet transform coefficients of supervised images in vertical and horizontal direction in three octaves. The framework proposed here is based on using wavelet transform modulus maxima to identify the maxima lines in a mammogram and extract the general modulus maximum gM from each maxima line. Simultaneously the algorithm determines the scale a_{gM} in which the general modulus maximum is detected. In the step that follows the algorithm searches for local magnitude minimum belonging to same maxima line in the scales a that satisfy $a > a_{gM}$ before the maxima line fades out. If it exists, the local magnitude minimum gm will be detected and corresponding scale $a_{gm} > a_{gM}$ will be determined. Singularities pointed by maxima lines with no identified minimums are considered as normal signal fluctuation and rejected from further analysis. Singularities with detected eligible minimums have negative Holder exponents. The fact that

described maximum and minimum are clearly detected means the log-log characteristic modulus maxima vs. scale has negative slope and isolated smoothed impulse function is localized at the point where maxima line propagates to scale $a = 1$. A maxima line might not propagate to a single point at scale $a = 1$ because of fast oscillations in the cone of influence around terminal point of the maxima line in the lowest detected scale. This location will be classified as an eligible singularity if the general maximum and its corresponding minimum are detected. An illustration of the framework is shown in Fig. 3.1.

Singular point selection is performed using a threshold value of magnitude of general maximum. Variance of smoothed impulse function can be estimated by the scale in which general maximum is detected [64]. This information will be employed in searching for eligible local intensity maximum around detected singularity in the process of microcalcification segmentation. If the intensity maximum doesn't exist, detected singularity should not be related to microcalcification. Similarly, additional information of the targeted singularity can be involved in further singularity sub-classification.

In this work I study magnitude and spatial distribution of general maxima of three different sets of the detected singularities in areas of diagnosed 25 microcalcification clusters:

1. All detected singularities which show negative Holder exponent which resemble smoothed impulse function,
2. The subsets of the set selected in 1 with dominant magnitudes of computed general maxima which resemble microcalcifications, and
3. The sets of singularities that correspond to diagnosed microcalcifications in 25 clusters.

Assuming that the nature of malignant and benign microcalcification clusters is different, I additionally study each category described above separately.

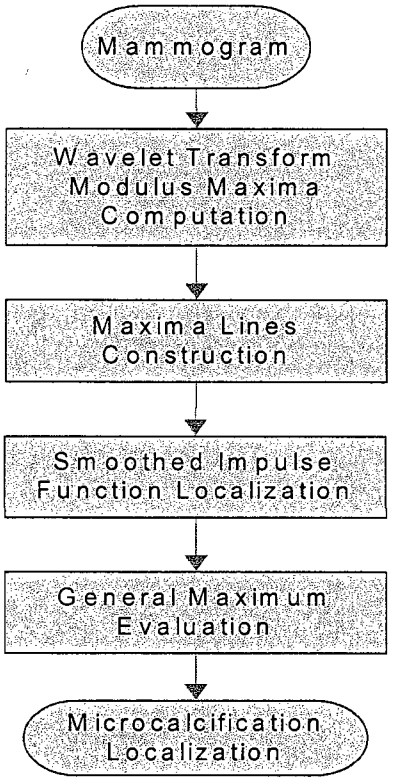

Figure 3.1. General maximum detection and microcalcification localization block diagram

Moreover, I investigate magnitude and spatial distribution of general maxima of three different sets of detected singularities in 20 healthy areas of same mammograms

4. All detected singularities which show negative Holder exponent and resembling smoothed impulse function in healthy areas and

5. The subsets of 4 that have dominant magnitudes of computed general maxima in healthy areas.

In this section, I describe the steps of the algorithm procedure presented in Fig. 3.1. Wavelet transform modulus maxima computation, maxima line construction, smoothed impulse function localization, and general maximum evaluation are discussed in separate sub-section. Blocks of size 128×128 pixels were taken from MIAS database [130] as the test mammograms. MIAS mammogram are digitized at 50 μm pixel edge and reduced to spatial resolution 200 μm pixel edge and clipped/padded so that every image is 1024 × 1024 pixels. The area of a pixel represents 0.04 mm^2 of breast tissue. Numerical resolution is 8 bits/pixel.

In this work the center of a cluster was chosen to be the center of the sub-image of 128×128 pixels. To prevent the border caused inaccuracy, the central part of a sub-image is used while the parts next to sub-image borders were excluded from further processing.

The algorithm parameters should be accordingly adjusted for other mammogram databases with different spatial and numerical resolution.

Wavelet Transform Modulus Maxima Computation

Although Mallat and collaborators [111] successfully applied spline based filter banks in dyadic wavelet transform for singularity detection, Arneodo et al. [126] suggested continuous wavelet transform to be performed with Gaussian kernel. Gaussian kernels and their derivatives are used to enable image processing with no particular bias in the space-scale analysis. Significant fractal properties can change very fast in scale. They often become invisible within less than a ½ of an octave and with

coarse scale increment the trend of modulus maxima behavior in scale could not be detected.

The scale is changing in three octaves covering all possible microcalcifications in mammograms with spatial and numerical resolution of MIAS database. Notice that three octaves cover scales from 1 to 8, i.e. microcalcification sizes in the range 0.2 to 1.6 mm. Scale change has been defined by

$$\sigma_{k+1}^2 = \sigma_k^2 \cdot (inc)^2 \tag{3.1}$$

where variance σ_0^2 of the Gaussian wavelet applied in initial scale $\boldsymbol{a} = 1$ and scale increment ***inc*** have empirically been determined to increase computational accuracy and convergence.

Gaussian Filter Coefficients

If smoothing function is Gaussian a modulus maxima must propagate toward finer scales along its maxima line [109].

A 2-D Gaussian smoothing function

$$\phi(x, y) = \frac{1}{2\pi\sigma^2} e^{-\frac{x^2+y^2}{2\sigma^2}} \tag{3.2}$$

of a scale independent size 31×31 pixels with initial variance σ_0^2 at scale $a_0 = 1$ is constructed and horizontal and vertical derivative are calculated per (3) and (4),

$$\psi_1(x, y) = \frac{\partial\phi(x, y)}{\partial x} \tag{3.3}$$

$$\psi_2(x, y) = \frac{\partial\phi(x, y)}{\partial y} \tag{3.4}$$

Discretization of a Gaussian smoothing function using (3.2) is typically achieved by sampling the Gaussian at discrete points corresponding to the central points of each pixel. The pixels at a distance of more than 3σ are small enough and often can be ignored. For the very small kernel filters, accuracy is maintained by integration of the Gaussian function over each pixel's area [131].

Computational Accuracy in Spatial and Frequency Domain

Wavelet coefficients computation may be performed with properly chosen filter coefficients in either spatial or frequency domain. The magnitude and location of the peak values of the 1-D Gaussian first derivative have been employed for the metrics of the accuracy assessment. The 9-tap Gaussian kernel with $\sigma = 1$ has yielded 76 % and 107 % of expected peak values of its first derivative at $\pm\sigma$, i.e. at ± 1, as shown in Fig. 3.2 (a) calculating in spatial and frequency domain respectively. Similarly, the 17-tap Gaussian kernel with $\sigma = 2$ has yielded 98 % and 100 % of expected peak values of its first derivative again at $\pm\sigma$, i.e. at ± 2 calculating in spatial and frequency domain respectively, as shown in Fig. 3.2 (b).

The experimental results presented in Fig. 3.2 show the advantage of computation in frequency domain particularly when smaller variance of Gaussian is employed.

Frequency Range

Wavelet reconstruction from Gaussian samples is performed to estimate both minimal variance and minimal filter length that may be acceptable in the terms of

computational accuracy. Minimal length of 3 taps and the variance $\sigma^2 = 0.25^2$ generally can't satisfy desired accuracy as shown in Fig. 3.3 (a). Filter lengths of 7 or more taps and a variance $\sigma^2 = 0.75^2$ generally satisfy the desired accuracy as shown in Fig. 3.3 (b).

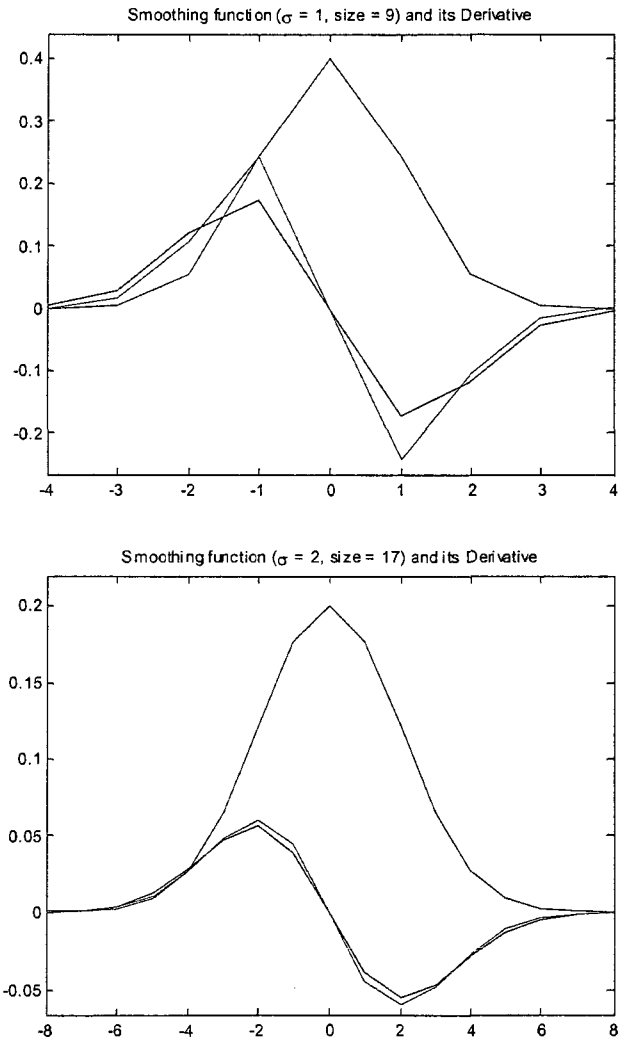

Figure 3.2. Red lines are filter coefficients calculated from Gaussian smoothing functions (red lines) with s = 1 - (a) and s = 2 - (b). The wavelet filter coefficients are calculated in time (blue) and frequency (purple) domain.

The lengths of 3 and 5 taps can satisfy desired accuracy in terms of localization because the peak values may match their locations but not their magnitude as shown in Fig. 3.3 (c) and Fig. 3.3 (d).

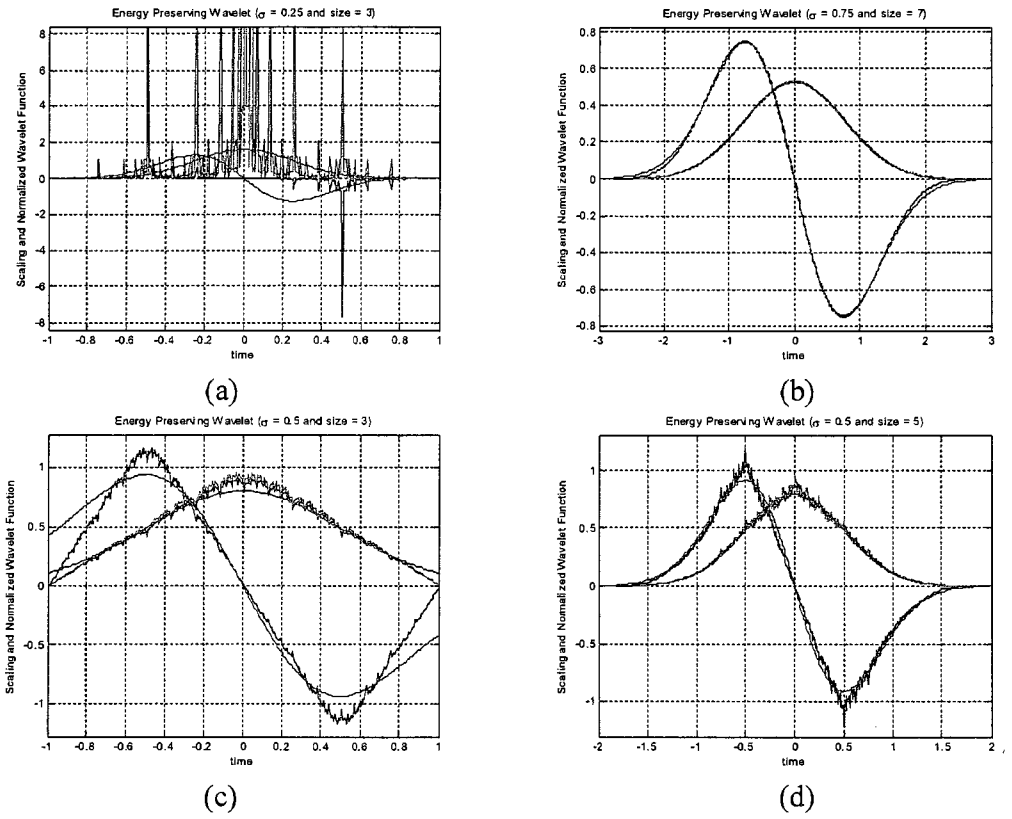

Figure 3.3. Reconstruction of 1-D scaling (green) and normalized wavelet (black) function for computation accuracy testing. The red lines are desired function performance, while accomplished scaling and wavelet functions are green and black lines respectively.

Energy Conservation

Filter coefficients of a Gaussian first derivative are normalized using the formula

$$M_a(x,y)=\frac{1}{\sqrt{C_\psi}}\sqrt{\left(W_a^{hor}\right)^2+\left(W_a^{ver}\right)^2} \tag{3.5}$$

The coefficient

$$C_\psi=(2\pi)^2\int\frac{|\psi(\omega)|^2}{|\omega|^2}d\omega \tag{3.6}$$

where $\omega=(\omega_{hor},\omega_{ver})$ and $|\omega|^2=\omega_{hor}\cdot\omega_{ver}$, enables the wavelet transform to be invertible i.e. $C_\psi<\infty$ represents admissibility condition. The admissibility condition $C_\psi<\infty$ means that the wavelet has a zero mean. Employing coefficient C_ψ improves modulus maxima analysis along a maxima line, i.e. smoothed impulse function and corresponding general maximum detection.

Maxima Line Construction

Each maxima line points to a singularity and each singularity is analyzed based on the modulus maxima behavior along its maxima line. Detected singularities gradually change in scale both the magnitude M and the argument θ of their modulus maxima. Two maxima points in two consecutive scale layers belong to same maxima line if their spatial locations and their arguments are similar. The level of similarity of their arguments is measured by empirically determined thresholds. The experiments show that the detection process converges if the scale increment in (1) between two consecutive scale layers is as low as $inc = 2^{1/16}$ [132]. Then the algorithm will properly

form a maxima line with the argument threshold $dA = \frac{\pi \cdot \log_2(inc)}{4} rad$ or $\Delta\theta < dA = \frac{\pi}{64} rad$ in the simulations presented in Chapter IV.

The procedure starts by connecting maxima points detected in the highest scales to the maxima points in adjacent scale layer below. When eligible connections are found for all maxima points in a scale layer the algorithm switches to adjacent scale layer below and repeats the connection search. The algorithm stops when it reaches the lowest scale in which the singularity is localized. The block diagram of maxima lines construction algorithm is presented in Fig. 3.4.

In some specific situations when maxima line switches from one point to another and both belong to the same feature, the argument difference can be significantly larger than the argument threshold and then magnitude threshold will be checked as an alternative to argument threshold. The magnitude threshold applied in the simulations presented in this work was $dM_{a0} = 3 \times abs(M_{a1}\text{-}M_{a2})$, where M_{a1} and M_{a2} are the modulus maxima detected in two higher consecutive scales as can seen in Fig 3.5.

Smoothed Impulse Function Localization

The singularities with positive Holder exponent have been considered as normal signal fluctuation, while negative Holder exponent is the feature of smoothed impulse function. The expected shape of the log-log characteristics of modulus maxima vs. scale is shown in Fig. 2.1 and Fig. 2.2. Negative Holder exponent is detected by negative slope of the characteristics in the scales above the scale $\boldsymbol{a_{gM}}$ in which general maximum $\boldsymbol{gM}$ was detected.

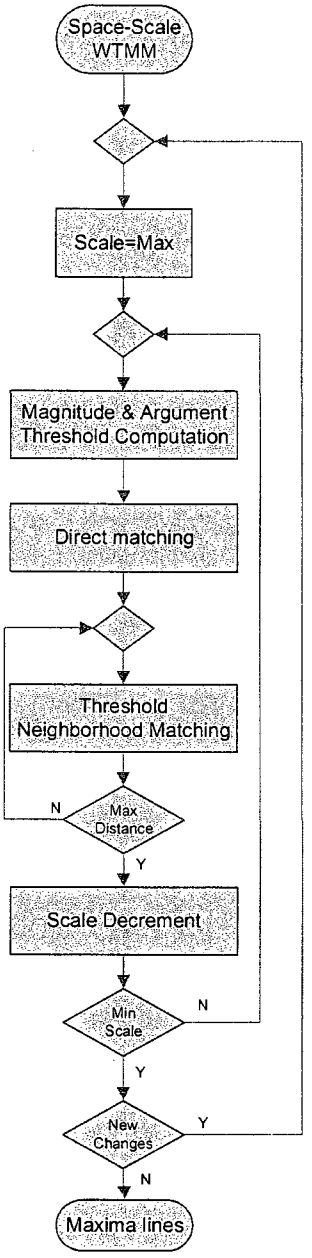

Figure 3.4. Maxima line construction block diagram

The algorithm first detects general modulus maximum gM and corresponding scale a_{gM} in a maxima line and then eligible minimum gm along the maxima line in the higher scales such that $a_{gm} > a_{gM}$. The distance in scale between two of them

$\Delta a = a_{gm} - a_{gM}$ must be large enough to show modulus decreasing tendency in higher scales, i.e. smoothed impulse function nature at the singularity pointed in the lowest scale of maxima line. In this work I consider $\Delta a \leq da$ where ***da*** = ¼ of an octave as a minimal distance between general modulus maximum and eligible minimum. This location will be classified as an eligible singularity.

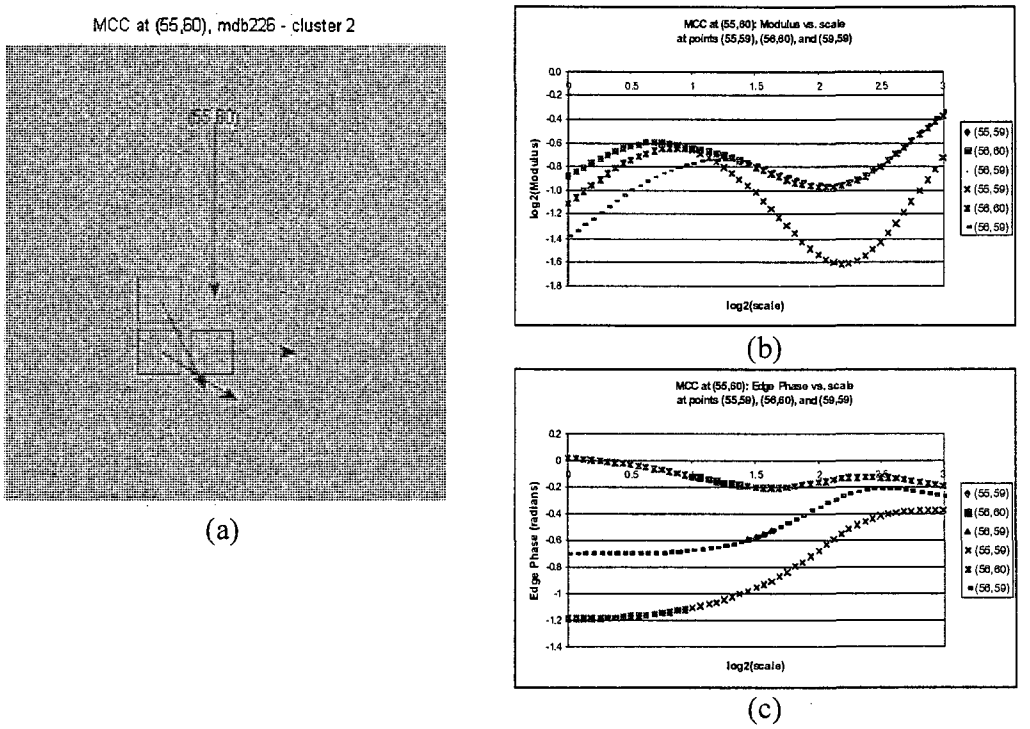

Figure 3.5. Example of maxima line construction from three singular points belonging to the same sharp transition. Three singular points around the pixel (55, 60), shown in (a), that can compose a maxima line as shown in bold and colored symbols in (b). Their arguments are significantly different representing the tangential directions of an edge around pixel (55, 60) but in higher scales they converge to the same limit as clearly illustrated in (c). Bolder symbols in the diagrams represent the values that belong to detected maxima line representing the same higher scale structure.

The scale a_{gM} in which general modulus maximum is detected determines the expected maximal spatial distance between the singularity and local intensity maximum. Notice that the singularities pointed by maxima lines with no identified eligible minimums are considered as normal signal fluctuation and excluded from further analysis. General maximum classification block diagram is presented in Fig. 3.6.

Adaptive frequency threshold can be an interesting extension for a future research.

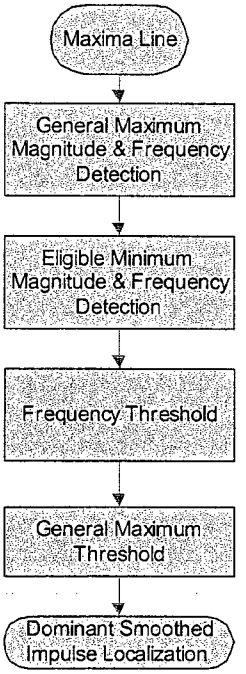

Figure 3.6. Integration of fractal dimension in the proposed framework to identify and classify the microcalcification related singularity

General Maximum Evaluations via Fractals

In this framework I propose to integrate general maximum average analysis and fractal dimension analysis for three different types of data of selected singularities

from abnormal tissue and two different types of data of selected singularities from healthy tissue. The results of fractal dimension computation show that dominant general maxima have similar fractal dimension for a given dataset as diagnosed microcalcifications supporting the assumption that the microcalcifications can be modeled as smoothed impulse function with dominant magnitude. This fractal dimension similarity approves that the spatial distribution nature of microcalcifications in mammograms is preserved general modulus maxima metric.

According to (2.13), fractal dimension of a selected set of singularities is determined as the negative value of the slope of log-log characteristics partition function $Z(q, a)$ vs. scale a with $q = 0$ as shown in Chapter 4 for each of the datasets proposed in Section 3.1.

Discussion

Continuous wavelet transform was employed to detect singularities in mammograms by tracking modulus maxima along maxima lines across the scale and integrating it with fractal dimension to differentiate between normal signal fluctuation and irregular ones in breast tissue.

In this work, microcalcifications in mammograms were modeled by smoothed impulse functions and detected by their negative Holder exponent. Proposed procedure for maxima line classification enables selected general maxima to be analyzed by their magnitudes.

The algorithm parameters should be carefully determined. For example, it was very difficult to determine an argument threshold that was able to result in consistent maxima line construction with scale increment as low as $\boldsymbol{inc} = 2^{1/4}$. In this work, I have used $\boldsymbol{inc} = 2^{1/16}$ instead. It is important to note that not only dyadic wavelet transform

cannot keep track of modulus maxima over scale but also scale increments of $2^{1/4}$ was not sensitive enough and experimental work indicated that it may be that there is no threshold value that will lead to convergence. In particular, the advantage of fast wavelet transform computation by quadrature mirror filter banks is not applicable because the dyadic wavelet transform is too coarse in both general maximum detection and Holder exponent computation.

This approach should be easily applicable to other mammogram databases with different spatial and numerical resolution if proper adjustment to the estimates of the parameters values were taken into consideration. It is important to note that, 1) argument threshold was fixed at low values enough to enable detection process to converge while compromising execution time, 2) frequency threshold was fixed low enough compromising false positive results, 3) modulus threshold were set to be adaptive, and 3) general maximum threshold was the average of eligible general modulus maxima to correlate between dominant general modulus maxima and the clinical diagnosis.

It is important to note that the slope measurement depends on the frequency range in which smoothed impulse function was recognized because only isolated and dominant singularities will have the frequency range wide enough to be recognized by the slope tending to -1.

CHAPTER IV

DETECTION PERFORMANCE ANALYSIS OF MICROCALCIFICATIONS IN DIGITIZED MAMMOGRAMS

The 25 sub-images of size 128×128 pixels were taken from MIAS database [130] covering the areas over the centers of the diagnosed microcalcification clusters along with other 20 healthy regions selected from the same mammograms are used.

Mammograms Used in this Work

In this work 12 malignant and 13 benign microcalcification clusters detected in 20 mammograms of MIAS database have been used. The clusters' information is presented in Table 1 as well as the details related to the tissue classification and type of disease per MIAS report [130].

Statistical Analysis of Singularities in Breast Tissue with Microcalcifications

In this work, a magnitude threshold of the general modulus maxima was determined as the local average of all gM of all eligible maxima lines with detected negative Holder exponent in the area 64×64 pixels centered in a diagnosed cluster. This choice of the threshold has reduced the number of dominant singularities (Table 2, columns 5 and 6) down to 31.1 % of all eligible singularities (Table 2, columns 3 and 4). I selected the regions with diagnosed microcalcifications and counted the number of maxima lines and computed the average of the general modulus maxima that correspond to the microcalcifications (Table 2, columns 7 and 8). Total

number of maxima lines in the regions with microcalcifications represents 37.8% of all detected eligible singularities.

Table 1

Microcalcifications information taken from MIAS database

Case	Mammogram	Cluster	Tissue	Disease	Radius	Center (row)	Center (column)
1	2	3	4	5	6	7	8
1	209	1	G	M	87	522	647
2	211	1	G	M	13	698	680
3	213	1	G	M	45	505	547
4	218	1	G	B	8	396	519
5	219	1	G	B	29	269	546
6	222	1	D	B	17	598	398
7	223	1	D	B	29	543	523
8	223	2	D	B	6	496	591
9	226	1	D	B	7	415	287
10	226	2	D	B	25	475	329
11	226	3	D	B	8	304	531
12	227	1	G	B	9	558	504
13	231	1	F	M	44	487	603
14	236	1	D	B	14	201	276
15	238	1	F	M	17	472	522
16	239	1	D	M	40	270	645
17	239	2	D	M	25	217	567
18	240	1	D	B	23	411	643
19	241	1	D	M	38	347	453
20	248	1	F	B	10	424	378
21	249	1	D	M	48	517	544
22	249	2	D	M	64	386	575
23	252	1	F	B	23	658	439
24	253	1	D	M	28	461	733
25	256	1	F	M	37	541	400

Tissue: Fatty-glandular (G), Dense-glandular (D), Fatty (F)
Disease: Malignant (M), Benign (B)

Detection results for each cluster, disease detection statistics, and detection performance are presented in Table 2, Table 3, and Table 4 respectively.

Table 2

Detection results in 25 clusters

Case	Mammogram	No. of eligible maxima lines	Threshold (average of eligible gM)	No. of dominant maxima lines	Average of dominant gM	No. of accurate maxima lines	Average of accurate gM
1	2	3	4	5	6	7	8
			$\times 10^{-5}$		$\times 10^{-5}$		$\times 10^{-5}$
1	209	129	4.09	45	5.61	69	4.15
2	211	124	4.01	41	5.29	23	5.01
3	213	94	4.42	27	6.76	46	4.72
4	218	136	3.71	47	4.83	10	5.28
5	219	122	5.47	24	13.63	66	6.24
6	222	118	3.88	36	5.55	36	4.15
7	223	148	4.57	49	6.80	86	4.83
8	223	143	4.13	52	5.57	9	7.16
9	226	169	5.33	30	12.69	11	5.46
10	226	140	3.58	56	4.32	75	3.64
11	226	75	3.49	26	4.34	12	4.40
12	227	115	3.63	35	4.94	9	5.70
13	231	149	3.96	49	5.58	93	4.17
14	236	98	3.62	35	4.64	19	4.12
15	238	121	4.09	40	5.60	27	4.97
16	239	141	3.59	44	4.67	73	3.64
17	239	103	3.68	37	4.63	52	3.67
18	240	25	3.62	6	5.40	12	3.87
19	241	121	5.28	45	8.04	71	5.96
20	248	147	4.12	27	7.93	12	11.10
21	249	121	5.23	34	9.25	63	4.92
22	249	176	3.96	56	5.49	98	4.05
23	252	146	4.58	37	7.89	75	5.03
24	253	105	3.53	40	4.34	56	3.61
25	256	149	3.84	52	5.09	76	4.08

In this work, 3115 maxima lines in 25 regions of size 64×64 pixels were considered eligible representation of smoothed impulse function. To estimate method performance the dominant maxima lines with general maximum above the local average were selected. Out of the 3115 maxima lines 970 (31.1%) were accepted after general maximum ***gM*** thresholding (were above the local average), while 1179 (37.8%) were representing either malignant or benign microcalcifications. The fact that the total true positively selected maxima lines (Table 4), yielding the detection sensitivity of 65.2%, 64.1%, and 67.1% for all, malignant, and benign clusters respectively, show that general maxima magnitude can be utilized as an important tool in microcalcification detection.

Table 3

Disease detection statistics in 25 analyzed clusters

Disease	No. of eligible Maxima lines	No. of dominant maxima lines	Column (3)/(2), %	No. of accurate maxima lines	Column (5)/(2) %
1	2	3	4	5	6
Total (all)	3115	970	31.1	1179	37.8
Total (malignant)	1533	510	33.3	747	48.7
Total (benign)	1582	460	29.1	432	27.3

Average magnitude of general maxima of microcalcification was 4.58×10^{-5}, while the average of all eligible maxima lines was 4.18×10^{-5}, leaving additional room for selection improvement based on the magnitude of general maxima. Similar conclusion holds for separately analyzed both malignant and benign clusters where average magnitudes corresponding to microcalcifications were 4.34×10^{-5} and

5.02×10^{-5} respectively while threshold averages were 4.12×10^{-5} and 4.23×10^{-5} respectively. The details of detection performance are given in Table 4.

Table 4

Microcalcification detection performance in 25 analyzed clusters

	All clusters		Malign. clusters		Benign clusters	
	No. of eligible maxima lines	%	No. of eligible maxima lines	%	No. of eligible maxima lines	%
1	2	3	4	5	6	7
Total eligible	3115	100	1533	100	1582	100
True classified	2504	80.4	1234	80.5	1270	80.3
False classified	611	19.6	299	19.5	312	19.7
True Positive	769	24.7	479	31.2	290	18.3
True Negative	1735	55.7	755	49.2	980	61.9
False Positive	201	6.5	31	2.0	170	10.7
False Negative	410	13.2	268	17.5	142	9.0

In the areas that included 12 malignant clusters (limited to the size of 64×64 pixels) in 10 mammograms, 1533 maxima lines were considered eligible and after average thresholding 510 (33.3%) were declared as microcalcifications. In the same cluster samples, 747 maxima lines (47.8%) were pointing to diagnosed malignant microcalcifications.

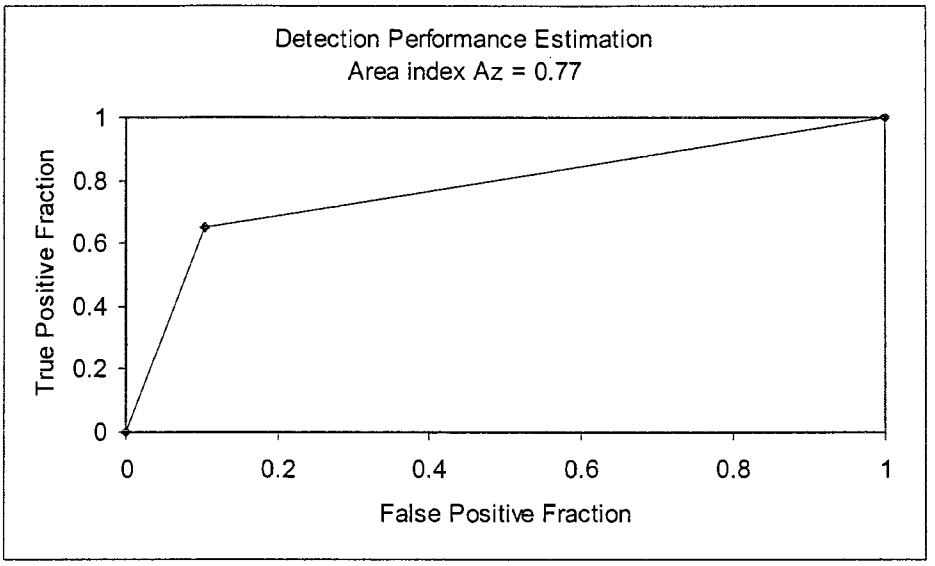

Figure 4.1. Area index estimation calculated from detection performance using local average threshold of general maxima

In the areas that included 13 benign clusters (also limited to the size of 64×64 pixels) in 10 mammograms, 1582 maxima lines were considered eligible and after average thresholding 460 (29.1%) were accepted as microcalcifications. In the same cluster sample, 432 maxima lines (27.3%) were pointing to diagnosed benign microcalcifications. The false positive and false negative detection results are shown in last two rows of Table 4.

Assuming that the average magnitude of general maxima was a threshold for detection classifier, the area index A_z representing detection performance for all cluster data in Table 4 was 0.77, as shown in Fig. 4.1. Similarly, area index A_z representing detection performance estimated separately for malignant and benign microcalcifications was 0.80 and 0.76 respectively.

Fractal Analysis of Singularities in Breast Tissue with Microcalcifications

Fractal dimension is originated from statistical mechanics. Fractal dimension can be estimated using the equations 2.12 and 2.13 when scale $a \to 0$. Having the mammogram data with finite resolution the requirement $a \to 0$ is reduced to $a \to 1$, i.e. $log(a) \to 0$. Saturation effect is caused by maxima lines with general modulus maxima detected in the lowest scales, in which the eligibility condition can not be clearly assigned to developed microcalcifications because coarse mammogram resolution allows detection of the microcalcifications themselves but not the properties in their borders.

For the purpose of computation accuracy of fractal dimension when the accuracy is higher if the sample data is larger, in the following sub-sections, the categories of data, rather than single clusters, were investigated:

1. All detected singularities that resemble smoothed impulse function in all analyzed microcalcification clusters, as well as separately in malignant and benign clusters.
2. The detected smoothed impulse functions with dominant general modulus maxima in all analyzed clusters, as well as separately in malignant and benign clusters.
3. The detected singularities that correspond to all diagnosed microcalcification clusters, as well as separately in malignant and benign clusters.

In all experiment, the end lines of the characteristics for all 25 clusters, 12 malignant clusters, and 13 benign clusters are determined in the range

$0.5 \leq \log_2(a) \leq 1.5$, where the characteristics are linear, showing their monofractals property. It is worth to notice that the characteristics show saturation effect in the range $0.0 \leq \log_2(a) \leq 0.5$, while in the range $1.5 \leq \log_2(a)$ the characteristics tend to diverge i.e. lose their linearity.

Eligible Singularities that Resemble Smoothed Impulse Functions

Log-log characteristics of partition functions $Z(q, a)$ vs. scale a, with $q = 0$, for all detected eligible singularities in 25 microcalcification clusters are shown in Figure 4.2. Specifically negative slopes of $\log_2(Z(0, a))$ vs. $\log_2(a)$, $0.5 \leq \log_2(a) \leq 1.5$, correspond to the fractal dimension of the sets of singularities for all detected singularities (rhombi), as well as for 12 malignant (squares) and 13 benign (triangles) clusters. The tend-lines show the slope is close to 2 in all three analyzed datasets. The results show that the eligible singularities are uniformly distributed everywhere in the analyzed mammogram subimages.

All Eligible Singularities above Average Threshold

Log-log characteristics of partition functions $Z(q, a)$ vs. scale a, with $q = 0$, for all detected eligible singularities with dominant general modulus maxima in 25 microcalcification clusters are shown in Figure 4.3. The negative slopes of $\log_2(Z(0, a))$ vs. $\log_2(a)$, $0.5 \leq \log_2(a) \leq 1.5$, correspond to the fractal dimension of the sets of singularities for all detected singularities (rhombi), as well as for 12 malignant (squares) and 13 benign (triangles) clusters. The tend-lines show the slope is

1.43, 1.46, and 1.40 for all three analyzed datasets, total, malignant, and benign respectively.

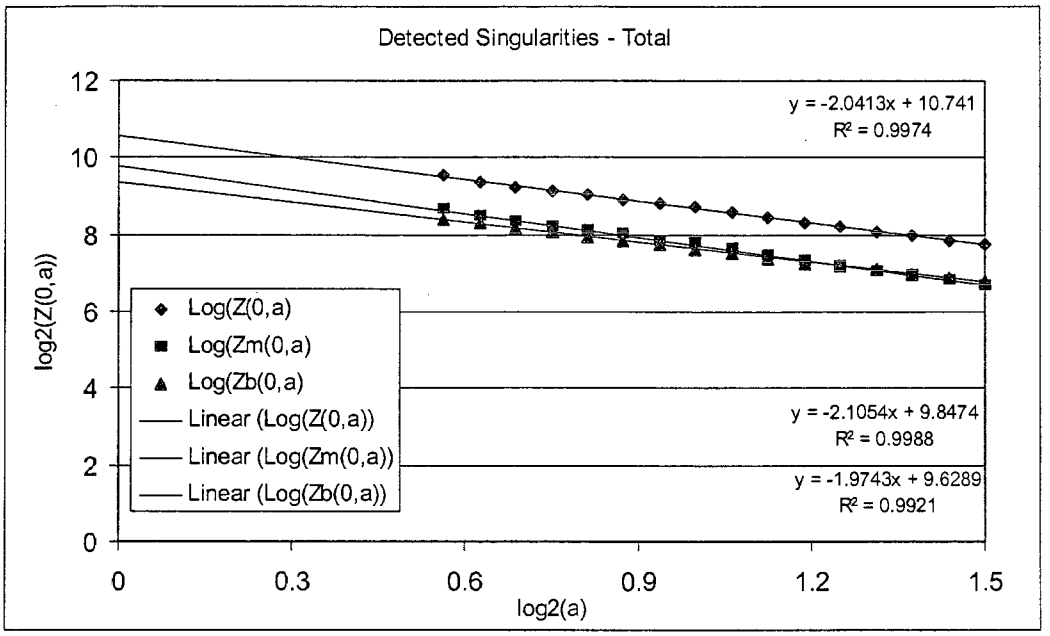

Figure 4.2. Partition function $Z(q, a)$ with $q = 0$, for all detected singularities in the 25 analyzed microcalcification clusters – rhombi. The squares and triangles represent partition functions for the detected singularities in the areas of malignant and benign clusters respectively. The fractal dimension in all three sets of data (the slope of the tend lines) is close to 2, showing that the singular points are distributed everywhere in the clusters.

MIAS Suggested Diagnosis

Log-log characteristics of partition functions $Z(q, a)$ vs. scale a, with $q = 0$, for all detected eligible singularities with dominant general modulus maxima in 25 microcalcification clusters are shown in Fig. 4.4. The negative slopes of $log_2(Z(0, a))$ vs. $log_2(a)$, $0.5 \leq log_2(a) \leq 1.5$, correspond to the fractal dimension of the sets of singularities for all detected singularities (rhombi), as well as for 12 malignant

(squares) and 13 benign (triangles) clusters. The tend-lines show the slopes are around 1.47 for all three analyzed datasets, total, malignant, and benign.

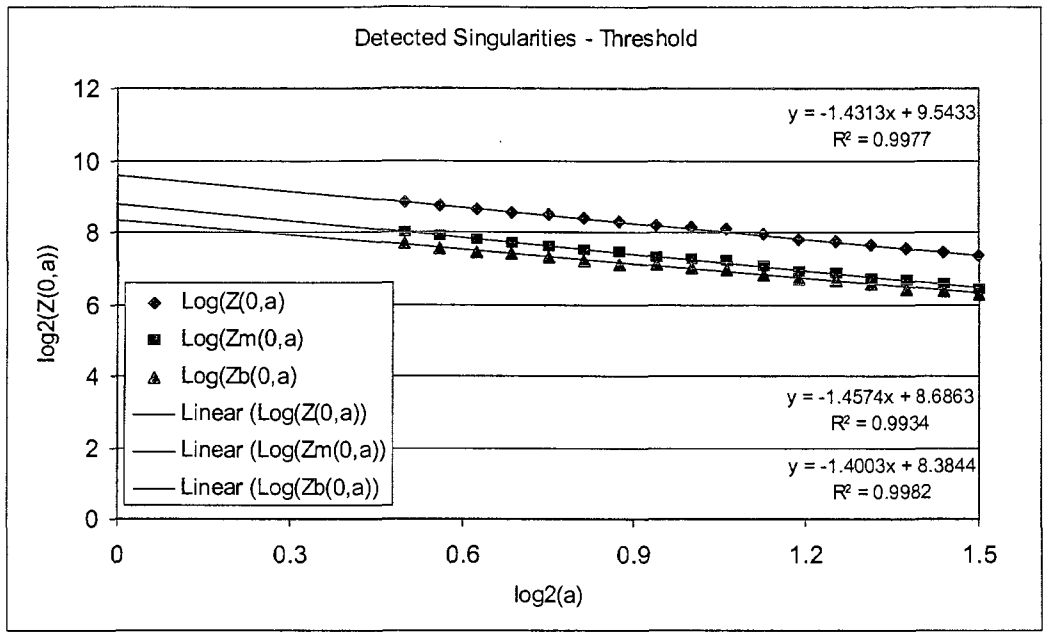

Figure 4.3. Partition function $Z(q, a)$ with $q = 0$, for all detected singularities above the local average in the areas of 25 analyzed microcalcification clusters – rhombi. The squares and triangles represent partition functions for the detected singularities in the areas of malignant and benign clusters respectively. The fractal dimension in all data sets (the slope of the tend lines) is 1.43, 1.46, and 1.40 for all, malignant, and benign detected dominant singularities respectively.

All three datasets yield fractal dimension of around 1.47, which is similar to the results of the thresholding, presented in Fig. 4.4. Fractal dimension of singularities selected by thresholding of all detected smoothed impulse functions and accurate microcalcification singularities are 1.43 and 1.46 and 1.40 for all, malignant, and benign microcalcification clusters respectively, supporting the assumption that

smoothed impulse functions with dominant general modulus maxima correspond to diagnosed microcalcifications.

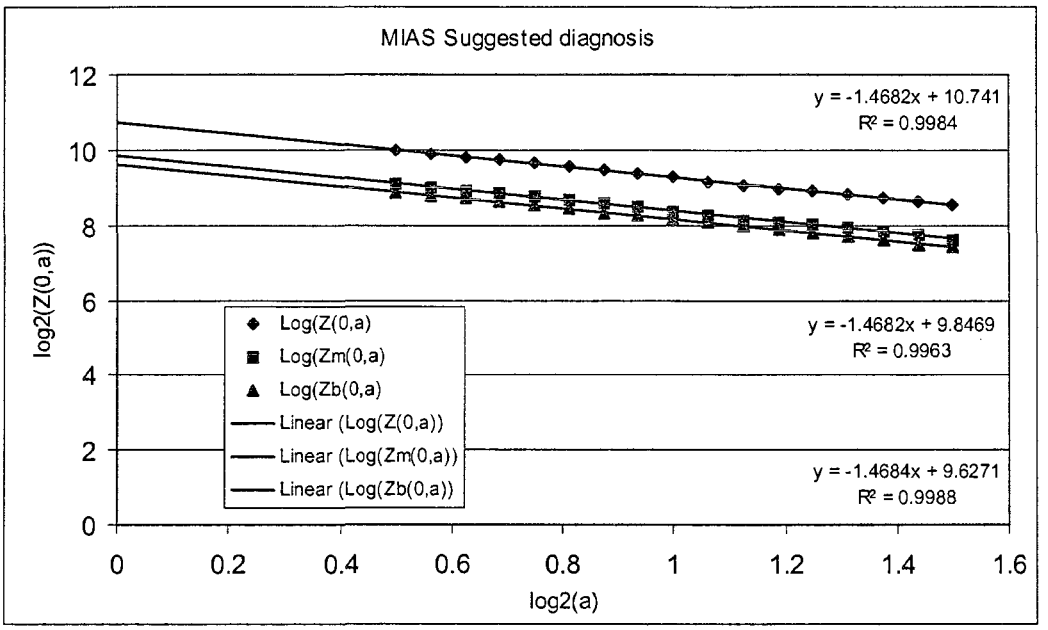

Figure 4.4. Partition function $Z(q, a)$ with $q = 0$, for all detected singularities pointing to diagnosed microcalcifications in the regions of 25 analyzed microcalcification clusters – rhombi. The squares and triangles represent partition functions for the detected singularities in the areas of malignant and benign clusters respectively. The fractal dimension in all three data sets (the slope of the tend lines) is 1.47 for all, malignant, and benign diagnosed microcalcifications respectively.

Healthy Tissue Analysis

For comparison purposes, 20 areas with no microcalcifications from each analyzed mammogram were selected and the general modulus maxima were tested. The information of selected areas is listed in Table 5 as well as the details related to the tissue classification.

Statistical Results of Healthy Tissue Analysis

The average of general maximum magnitude in areas with microcalcification clusters is higher than the averages with no clusters. The average of detected general modulus maxima in the areas of 64×64 pixel in healthy tissue areas was in the order of 3.6×10^{-5} with about 120 eligible maxima lines. Similar results were produced for all three types of analyzed tissue, i.e. 3.6×10^{-5}, 3.5×10^{-5}, and 3.7×10^{-5} with fatty-glandular, dense-glandular, and fatty tissue respectively. This result shows that proposed metric is not sensitive on background tissue.

The results for each mammogram are presented in column 10 of Table 6. For each mammogram, number of detected dominant singularities and their average general maximum in the area with microcalcification cluster is compared to data of selected area without microcalcifications. Columns 6 and 10 in Table 6 represent increase rate in the number of detected dominant singularities and average magnitude of general maxima, respectively. Randomly chosen samples caused the exception in the case of mammograms mdb226 and mdb227 with benign microcalcification clusters. Columns 6 and 10 approve that the areas with microcalcifications have more dominant smooth impulse function singularities and their average is larger than in the case without microcalcification clusters. In future work, both local and global averages should be analyzed for optimum threshold selections.

When average criterion was used then 37.3% false positive results were produced. False positive rate doesn't change significantly in all three types of tissue, i.e. 35.6%, 38.3%, and 37.8% with fatty-glandular, dense-glandular, and fatty tissue

respectively. If a requirement for presence of a local intensity maximum in the neighborhood of a singularity was applied the false positive rate detection fell down to 17.5%, i.e. 15.2%, 17.8%, and 19.2% with fatty-glandular, dense-glandular, and fatty tissue respectively. This result implies low sensitivity of proposed metric on background tissue.

Table 5

List of mammograms from MIAS database with selected testing areas without microcalcifications (healthy tissue)

Case	Mammogram	Tissue	Center (row)	Center (column)
1	2	4	5	6
1	209	G	394	519
2	211	G	570	552
3	213	G	633	547
4	218	G	524	519
5	219	G	397	418
6	222	D	726	526
7-8	223	D	671	651
9-11	226	D	543	415
12	227	G	686	632
13	231	F	615	731
14	236	D	329	404
15	238	F	600	522
16-17	239	D	398	645
18	240	D	539	515
19	241	D	475	453
20	248	F	552	506
21-22	249	D	645	672
23	252	F	530	439
24	253	D	589	605
25	256	F	669	528

Tissue: Fatty-glandular (G), Dense-glandular (D), Fatty (F)

Table 6

Statistical results of healthy tissue analysis detection results in 20 healthy areas of 64×64 pixels

Case	Mamm ogram	No. of eligible max. lines	Thresh (all max. lines)	Thresh (all max. lines)	Col. (4)/(5)	No. of accept. max. lines	Aver. of dom. gM	Aver. of accur. gM	Col. (8)/(9)
1	2	3	4	5	6	7	8	9	10
			$\times 10^{-5}$	$\times 10^{-5}$	%		$\times 10^{-5}$	$\times 10^{-5}$	%
			healthy	mcc			healthy	mcc	
1	209	79	3.13	4.09	77	28	3.60	5.61	64
2	211	124	3.69	4.01	92	46	4.51	5.29	85
3	213	112	3.82	4.42	86	29	5.65	6.76	84
4	218	120	3.27	3.71	88	44	3.86	4.83	80
5	219	80	3.49	5.47	64	32	4.24	13.63	31
6	222	120	3.53	3.88	91	45	4.30	5.55	77
7-8	223	157	3.40	4.13	82	68	3.95	5.57	71
9-11	226	159	3.78	3.49	108	62	4.72	4.32	109
12	227	143	3.76	3.63	104	53	4.75	4.94	96
13	231	194	3.74	3.96	94	69	4.77	5.58	85
14	236	48	3.23	3.62	89	12	4.25	4.64	92
15	238	149	3.60	4.09	88	58	4.32	5.60	77
16-17	239	95	3.24	3.59	90	37	3.78	4.63	82
18	240	0	N/A	3.62	N/A	0	N/A	5.40	N/A
19	241	53	3.05	5.28	58	20	3.45	8.04	43
20	248	140	3.81	4.12	92	55	4.71	7.93	59
21-22	249	183	3.79	3.96	96	66	4.82	5.49	88
23	252	171	3.82	4.58	83	67	4.70	7.89	60
24	253	56	3.07	3.53	87	23	3.43	4.34	79
25	256	138	3.57	3.84	93	50	4.45	5.09	87

Fractal Analysis of Healthy Tissue

In this sub-section fractal dimension for two data sets, all eligible singularities and dominant singularities, are analyzed separately.

All detected singularities that resemble smoothed impulse function are analyzed

first. The fractal dimension of the detected smoothed impulse functions in all 20 healthy areas was 1.73 which is lower than 2.0 determined in breast areas with microcalcifications. Notice that a fractal dimension approaching 2 is a sign that normal signal fluctuation is present everywhere in the plane.

Partition function and its linear regressions of all detected singularities in healthy area are presented in Fig. 4.5.

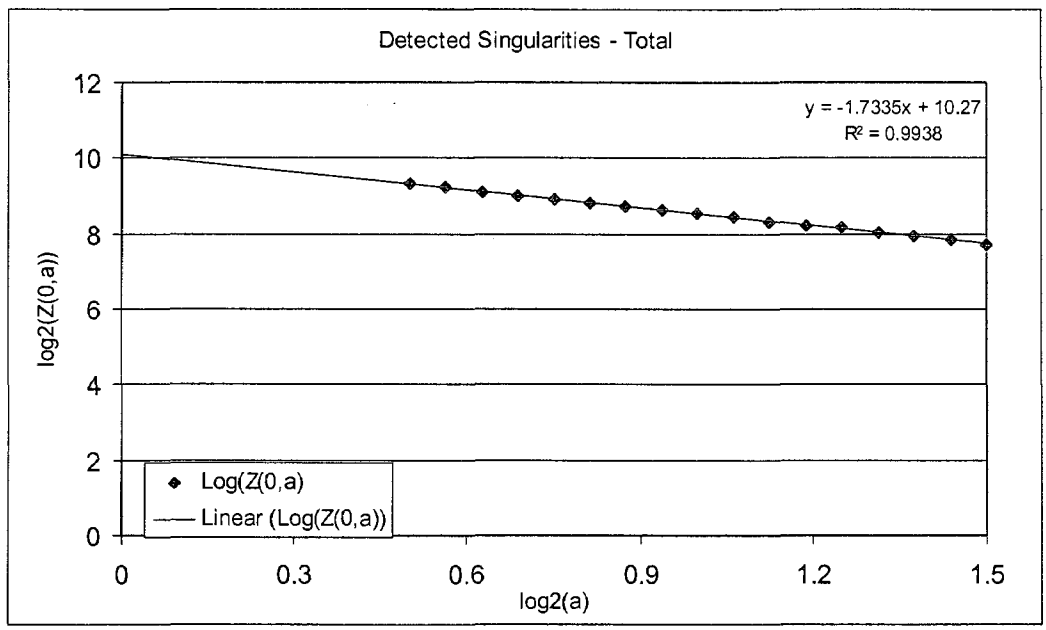

Figure 4.5. Partition function $Z(q, a)$ with $q = 0$, for all detected singularities in the 20 analyzed mammograms. The fractal dimension (the slope of the partition function, $q = 0$ and $a \rightarrow 0$) for 20 healthy areas is 1.73 - linear regression slope.

Dominant singularities in healthy areas have significantly lower fractal dimension, i.e. tending to 1 for the average of all 20 mammograms. Fractal dimension approaching 1 is the sign of linear structures typical for detected edges. Fractal

analysis shows that smoother signal transition is uniformly distributed everywhere producing fractal dimension tending to 2 in both normal and abnormal breast tissue. On another hand fractal dimension of detected dominant signal transition in normal tissue is tending to 1 implying that they belong to the line structures. Partition function and its linear regressions of dominant singularities in healthy area are presented in Fig. 4.6.

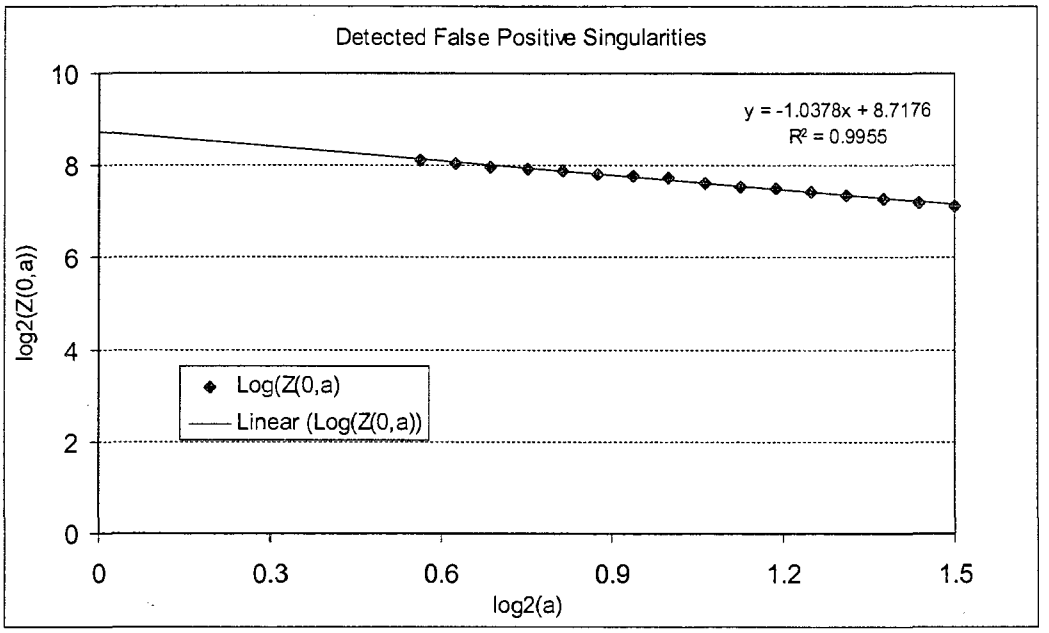

Figure 4.6. Partition function $Z(q, a)$ with $q = 0$, for all detected singularities above the average magnitude in the 20 analyzed mammograms. The fractal dimension (the slope of the partition function with $q = 0$) is 1.03, - linear regression slope.

Healthy tissue fractal analysis shows that the set of all detected singularities has fractal dimension of 1.73 while the set of locally dominant singularities has fractal dimension tending to 1. This is in agreement with the results on the significance of

general modulus maxima in the detection of microcalcification. Fractal dimension of 1 is typical for the linear structures in the tissue and can be used in mammogram segmentation which can be a future extension of this work.

Healthy tissue statistical analysis confirms our expectation that general maxima of normal fluctuation with negative Holder exponent are lower than the general maxima belonging to the maxima lines representing the abnormalities suggesting that a combination of global and local thresholding need to employed.

Notice that for microcalcification cluster classification purposes spatial resolution of 200μm doesn't allow zooming at 70μm where microcalcification edge becomes visible and malignancy analysis possible.

Detection Result Example

Our proposed algorithm successfully localized both malignant and benign microcalcification clusters and it is worthy to notice that no other features but dominant general modulus maximum with average threshold is employed in the detection of microcalcification clusters such as those shown in Fig. 4.7 and Fig. 4.8.

Discussion

Detection sensitivity for all, malignant, and benign clusters were 65.2%, 64.1%, and 67.1% respectively, while area index A_z was 0.77, 0.80, and 0.76 respectively, implying that general maxima magnitude can be utilized as an important tool in microcalcification detection.

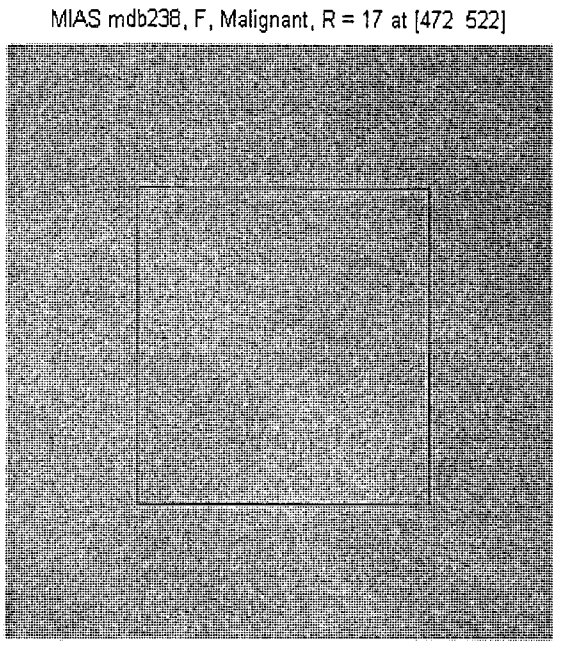

(a)

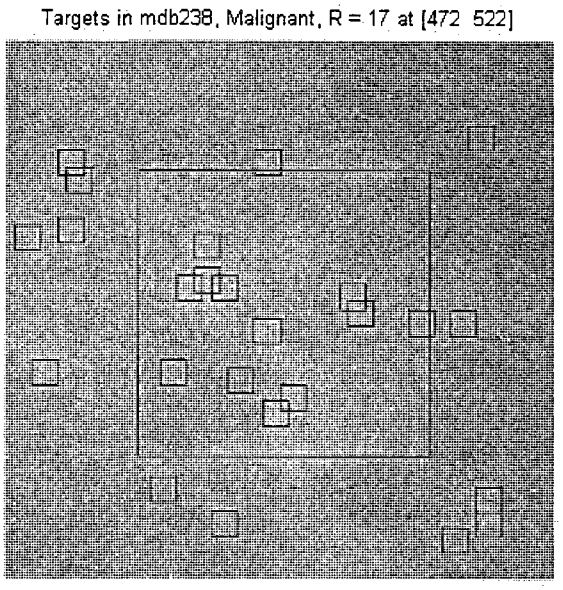

(b)

Figure 4.7. A malignant microcalcification cluster of radius R = 17 pixels is diagnosed in the area bordered by black squared line in the mammogram MIAS mdb238 – Fig. 4.7 (a). The centers of highlighted squares in Fig. 4.7 (b) are detected dominant singularities resembling smoothed impulse functions.

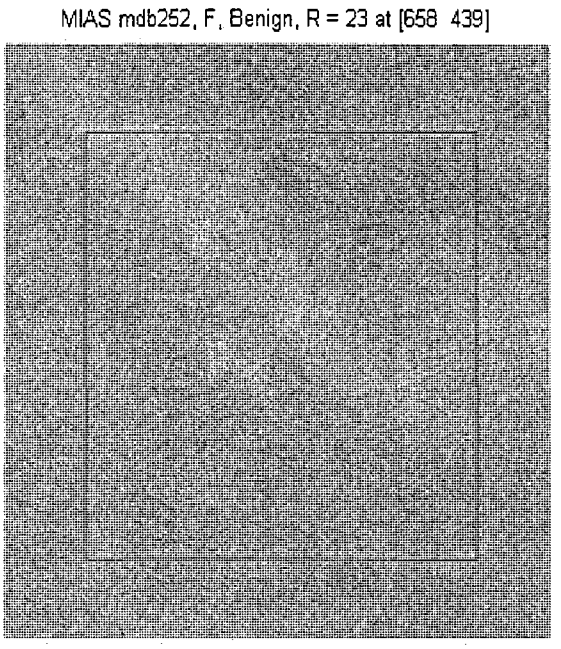

(a)

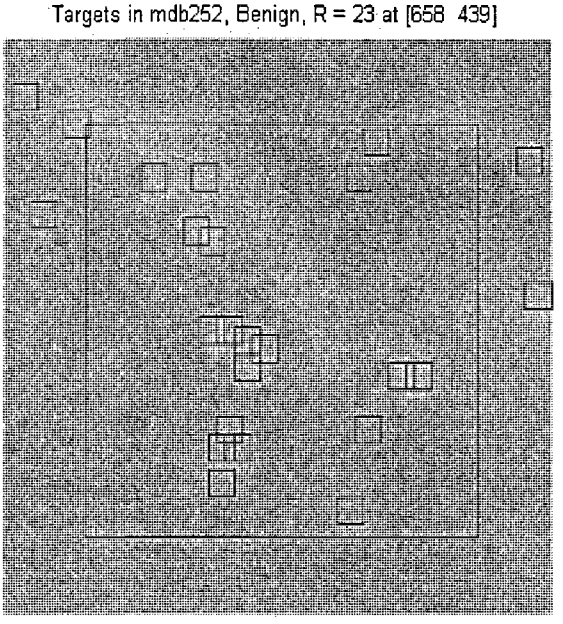

(b)

Figure 4.8. A benign microcalcification cluster of radius R = 23 pixels is diagnosed in the area bordered by black squared line in the mammogram MIAS mdb252 – (a). The detected dominant singularities resembling smoothed impulse functions shown as the centers of bordered area - (b).

Average magnitude of general maxima in the healthy regions was 3.6×10^{-5}, 3.5×10^{-5}, and 3.7×10^{-5} with fatty-glandular, dense-glandular, and fatty tissue respectively. When average criterion was used then 37.3% false positive results were produced in the healthy regions. False positive rate doesn't change significantly in all three types of tissue, i.e. 35.6%, 38.3%, and 37.8% with fatty-glandular, dense-glandular, and fatty tissue respectively. Very similar statistical results, including the number of 120 detected eligible maxima lines (per area of 64×64 pixels) in all three types of analyzed healthy tissue imply that proposed metric is not sensitive on the background tissue. This is very important because microcalcification detection in dense parenchyma can be particularly challenging task.

Average magnitude of general maxima of microcalcifications was 4.58×10^{-5}, while the average of all eligible maxima lines in the same regions was 4.18×10^{-5} vs. 3.6×10^{-5} in healthy regions, leaving additional room for selection improvement based on the magnitude of general maxima.

Average threshold for malignant and benign clusters was 4.12×10^{-5} and 4.23×10^{-5} respectively, having relative difference in the order of 2.5 %, while average magnitude of benign microcalcifications was 13.6% higher than average magnitude for malignant microcalcification (4.34×10^{-5} and 5.02×10^{-5} respectively). The average threshold generated significantly less false positive than false negative malignant findings (2.0% vs. 17.5%), which was not the case with benign findings (10.7% vs. 9.0%). This statistics implies that general modulus maxima of malignant findings might be detected in lower scales. Further investigation of possible differences

between malignant and benign calcification should be focused on the detection parameters in the lower scales.

Both log-log characteristics modulus maxima vs. scale and partition function vs. scale are smooth allowing reliable threshold selections in the singularity classification process. The results of fractal dimension computation show that dominant general maxima have similar fractal dimension for a given dataset as diagnosed microcalcifications supporting the assumption that the microcalcifications can be modeled as smoothed impulse function with dominant magnitude. This fractal dimension similarity approves that the spatial distribution nature of microcalcifications in mammograms is preserved by general modulus maxima metric.

Dominant general modulus maxima highly map into diagnosed microcalcifications in terms of average magnitude and spatial distribution. Simulation results demonstrated that smoothed impulse function, recognized by their fractal properties of localized wavelet transform modulus maxima, can be considered a reliable feature for microcalcification detection in mammograms. Moreover, comparison of healthy and calcified breast tissue based on both statistical and fractal results show that selected general modulus maximum is a significant feature in microcalcification detection and classification. The results show that proposed metric for microcalcification detection is not sensitive on background tissue and particularly convenient for dense parenchyma background. It also worthy of noting that the implementation of this proposed work including all parameter values is appropriate for the 200 μm/pixel spatial resolution and 8 bits/pixel numerical resolution.

CHAPTER V

DETECTION OF MICROCALCIFICATION FRAMEWORK INTEGRATING SPATIAL FREQUENCY LOCALIZATION AND SEGMENTATION

Using magnitude of general maxima of smoothed impulse function in previous chapter I detected singular points that are candidates for microcalcifications in mammograms. High sensitivity of the algorithm yields high false positive results which is a deciding factor on the viability of using this algorithm as a computer aided detection tool.

In this chapter, I would like to show that (1) a microcalcification cluster can be located by energy blob of selected dominant general modulus maxima and (2) false positive and false negative single microcalcification findings can significantly be reduced by incorporating additional knowledge about target. Microcalcification is a residual calcium deposit causing higher X-ray attenuation and appearing as a spot brighter than its surrounding. Thus, in the area of a microcalcification, a pixel with local intensity maximum must exist.

Microcalcification Cluster Detection

Wang and Karayiannis [108] suggested detection of high frequency energy blobs with no differentiation between sharp transition characterized as smoothed impulse function and normal high frequency signal fluctuation in mammograms.

For the selection of the suspicious spots in mammograms I propose detection of energy blobs of dominant general modulus maxima. This simple procedure will be explained in detail by following detection procedure performed on mammogram

mdb223 [130] with two benign microcalcification clusters and a film damage as shown in Fig. 5.1. Notice that missing of local intensity maximum in the neighborhood of the sharp transition in the border of film damage caused elimination of related singular points from energy blob analysis.

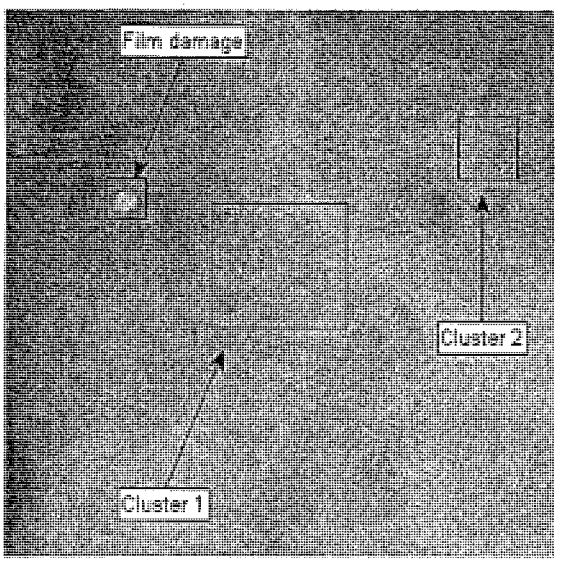

Figure 5.1. Mammogram mdb223 with two microcalcification clusters and a film damage

The input for energy blob detection is an image consisting of detected dominant smoothed impulse function shown in Fig. 5.2 - (a). Singularities with a local intensity maximum in the neighborhood are selected and represented by their magnitudes of general maxima.

A result of low-pass filtering of image in Fig. 5.2 – (a) is shown in Fig. 5.2 - (b). Applied filter was averaging non-zero magnitudes from Fig. 5.2 – (a). The size of the filter applied in Fig. 52 - (b) was 48×48 pixels.

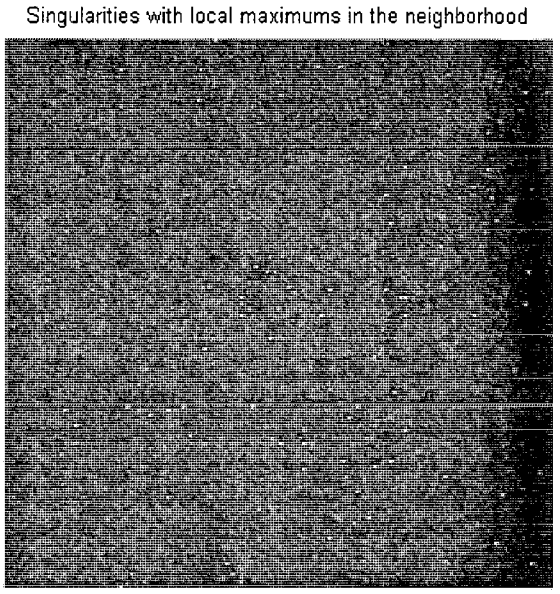

(a)

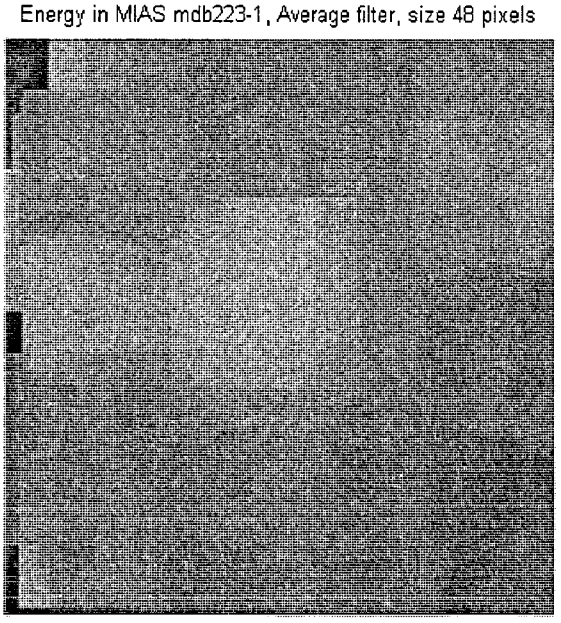

(b)

Figure 5.2. Detected dominant singularities with local intensity maximums in the neighborhood – (a), detected energy blobs, filter size 48×48 pixels – (b)

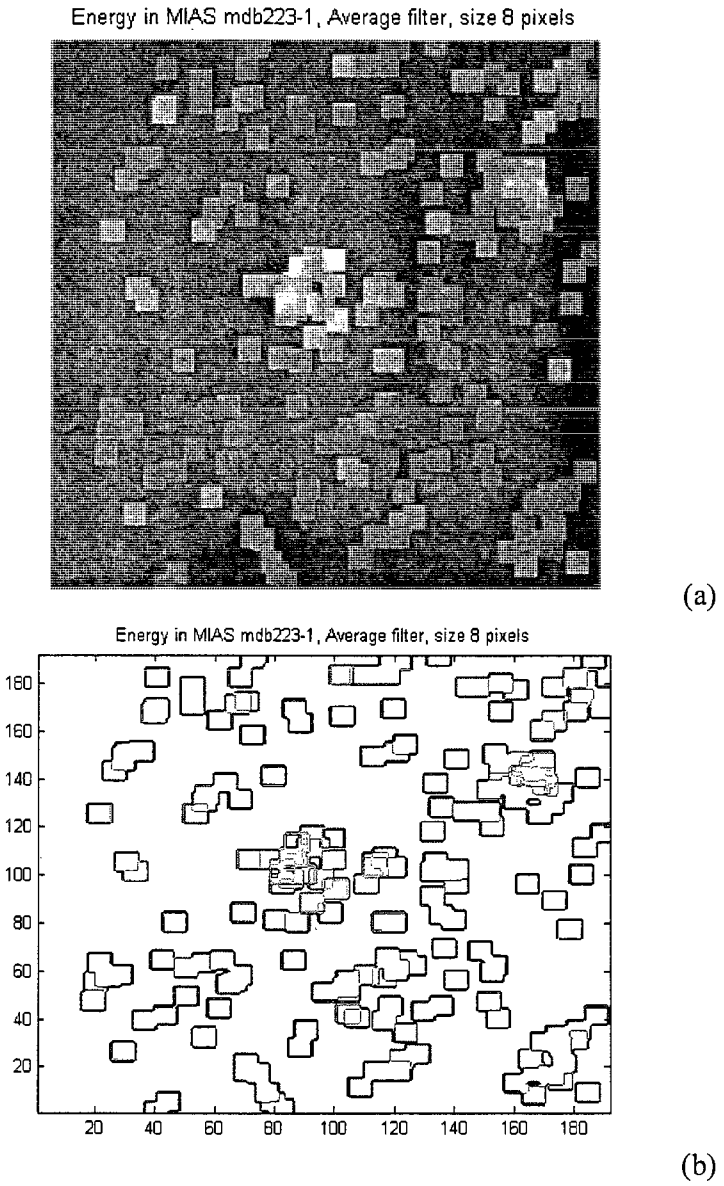

Figure 5.3. Detected energy blobs, filter size 8×8 pixels – (a), significant energy peaks are represented by yellow-orange-red isoenergy lines – (b)

Both larger cluster 1 and smaller cluster 2 are represented with areas locally brighter than its neighborhood as shown in Fig. 5.2 – (b). Film damage was not

disturbing the detection process, because of missing local maximums in the eligible neighborhood of the detected singularities in the border of film damage.

The procedure is repeated with a filter size of 8×8 pixels as shown in Fig 5.3.

Microcalcification Segmentation

The microcalcification clusters were located in Section 5.1. In this section the single microcalcifications will segmented by procedure that follows.

A detected eligible singular point s is located in the edge of the microcalcification where the signal transition is sharpest. Accepting the simplification that microcalcification is an ellipsoid, its radiuses are in the order of standard deviation of located smoothed impulse function.

Region Growing Segmentation Method

In this section I give short description of region growing segmentation method. Region growing method can be classified as one of the pixel-based image segmentation because it involves the selection of initial seed point.

This approach to segmentation examines the neighboring pixels of the initial seed point and determines the level of similarity to the seed point. The level of similarity is previously defined cost function which will allow or prevent a neighborhood pixel to be added to the pixel set that belongs to the region of the seed point. In next iteration the region will be allowed to grow from the pixels added to the region in previous iteration. The process is terminated when in last iteration no pixels are added to the regions that grow.

The region growing segmentation methods can correctly separate the regions that have the same previously defined properties. They can provide the original images which have clear edges particularly if applied multiple criteria at the same time. A weakness of the methods is the computation is consuming. Noise or variation of intensity may result in holes or over-segmentation, which can be prevented by using some mask to filter the holes or outlier.

An illustration of developed segmentation method is presented in Fig. 5.4.

Region Growing Seed Point

Region growing seed point $\boldsymbol{c}$ is determined as local intensity maximum in the 8-connected neighborhood of an eligible singularity $\boldsymbol{s}$. The radius of the neighborhood can be estimated from standard deviation of smoothed impulse function which depends on the scale in which the general maximum is detected, i.e. $\sigma = 2\sqrt{2} \cdot \beta \cdot a$ [64]. An eligible local maximum defined by (1) is detected in the distance less than standard deviation of smoothed impulse function from detected eligible singular point, i.e.

$$c(x_c, y_c) = \begin{cases} 1 & S_a(x_c, y_c) = \max\limits_{(x,y)\in\aleph_s} S(x,y) \\ 0 & otherwise \end{cases} \tag{5.1}$$

where $\boldsymbol{S}$ is input mammogram and $\aleph_s$ is a part of 8-connected neighborhood surrounding singularity $\boldsymbol{s}$ by diameter that corresponds to the scale $\boldsymbol{a_{gM}}$ in which general modulus of singular point s was detected.

For the microcalcification segmentation purpose the local maximum is convenient to be a seed point in a region growing segmentation procedure.

Dual Point

When a general modulus maximum is detected in scale ***a,*** its wavelet transform argument will point to the direction of the sharpest 2-D signal transition. It is accepted assumption that the smoothest change or edge will point to the direction orthogonal to the modulus maximum argument. Following the angle that is orthogonal on the local wavelet argument, edge detection in the scale ***a*** can be achieved. The microcalcification might not be dominant local structure that detected edge would follow. Having the seed point and the singularity incorporated in the edge I estimate a location of the edge on the opposite side of the ellipsoid by

$$d^* = c - \vec{cs} \tag{5.2}$$

where d^* is temporary dual point, c is location of local intensity maximum of underlying mammogram and $\vec{cs}$ is a vector representing the distance from seed point c and singularity s. I define dual point of the singularity as a point d with largest wavelet transform coefficient magnitude in the neighborhood of the estimated location d^*, i.e.

$$d(x_d, y_d) = \begin{cases} 1 & W_a(x_d, y_d) = \max\limits_{(x,y)\in \aleph_{d^*}} W_a(x,y) \\ 0 & otherwise \end{cases} \tag{5.3}$$

The dual point will be assigned as a point belonging to the edge on opposite side of the detected singularity.

Edge Detection

Argument of wavelet coefficients points the direction in which the signal change is maximal. The assumption here is that the direction in which the change is minimal is orthogonal to the direction of the sharpest transition. I construct the edges

in scale a by spreading the singularity and its dual point in the direction of

$$\theta_{edge}(x,y) = \arg(W_a(x,y)) \pm \frac{\pi}{2} \tag{5.4}$$

Spreading Limitation

In higher scales, constructed maxima chains will follow dominant in scales image structures. In accordance to the expectation of the size of a microcalcification i.e. the scale $a_s=a_{gM}$ in which corresponding general modulus maximum of the singularity is detected, I stop initial edge detection after a number of iterations that correspond to the scale a_s.

Segmentation Process

The segmentation process developed in this work is based on employing spatial (gray-scale values) and wavelet transform coefficients magnitude at the scale in which a singularity is detected, in a region-growing manner, to generate the segmented microcalcification. This is framework allows for other microcalcification features to be incorporated in the model. In general, models may include any characteristics such as homogenous regions in the image, objects of certain shapes, or of specific texture [133]. The more constraints are imposed, the more the algorithm is application dependent. In this work the input information are magnitude of wavelet transform coefficients computed for every pixel in scale a_{gM} and intensities of the underlying mammogram. The algorithm is initiated by accepting the results of the spatial-frequency singularity localization in 2-D signals explained in the previous section.

The algorithm follows singularity detection as described in Chapter III.

(1) Translate wavelet coefficient magnitudes in the detected scale to set a general modulus maximum to be positioned at the location of corresponding singular point s in the lowest scale.

(2) Locate a local intensity maximum c of underlying mammogram to be a seed point. If there is no local intensity maximum in the scale a_{gM} dependent neighborhood of singular point s, singular point s is not related to a microcalcification and segmentation process is terminated.

(3) Having the seed point as a reference point, determine temporary dual point on opposite side of the microcalcification local maximum by (5.2) and then localize the dual point with maximal modulus maximum in the 8-connected neighborhood of temporary dual point per equation (5.3).

(4) Starting from singularity and its dual point, perform initial microcalcification edge detection following wavelet transform argument per (5.4);

(5) Determine maximal area that a region can grow by spreading initial edges and seed point to their 8-connected neighborhood repeating the spreading up to the scale limitation.

(6) Modify wavelet coefficient magnitude using the formula

$$\left|W_{a\_m}(x_0,y_0)\right| = \frac{8\left|W_a(x_0,y_0)\right| + \sum_{(x,y)\in\aleph_e(x_0,y_0)}\left|W_a(x,y)\right|}{8+n_e(x,y)} \qquad (5.5)$$

where $\aleph_e(x_0, y_0)$ is the part of 8-connected neighborhood of (x_0, y_0) in which

$$|W_a(x,y)| > |W_a(x_0,y_0)| \tag{5.6}$$

and n_e is number of the neighborhood magnitudes satisfying the condition (5.6), while $a=a_{gM}$ is the scale in which general maximum of the singularity is detected.

(7) Compute the wavelet transform coefficient magnitude average and its standard deviation of 8-connected neighborhood i.e.

$$|W_{a\_mean}(x_0,y_0)| = \frac{\sum_{(x,y)\in N(x_0,y_0)} |W_a(x,y)|}{8} \tag{5.7}$$

and

$$|W_{a\_std}(x_0,y_0)| = \sqrt{\frac{1}{7}\sum_{(x,y)\in N(x_0,y_0)} \left(|W_a(x,y)| - |W_{a\_mean}(x_0,y_0)|\right)^2} \tag{5.8}$$

where $|W_{a\_mean}(x_0,y_0)|$ and $|W_{a\_std}(x_0,y_0)|$ are the neighborhood average and standard deviation of wavelet transform coefficients at (x_0,y_0) in scale $a=a_{gM}$ respectively.

(8) Compute the average intensity and its standard deviation of underlying of 8-connected neighborhood

$$I_{mean}(x_0,y_0) = \frac{\sum_{(x,y)\in N(x_0,y_0)} I(x,y)}{8} \tag{5.9}$$

$$I_{a\_std}(x_0,y_0) = \sqrt{\frac{1}{7}\sum_{(x,y)\in N(x_0,y_0)} \left(I_a(x,y) - I_{a\_mean}(x_0,y_0)\right)^2} \tag{5.10}$$

(9) Each pixel adjacent to the growing region of a microcalcification add to the growing region if satisfies (5.11) and (5.12)

$$\left|W_{a\_m}(x_0,y_0)\right| \geq W_{a\_mean}(x_0,y_0) + k_W W_{a\_std}(x_0,y_0) \tag{5.11}$$

and

$$\left|I(x_0,y_0)\right| \geq I_{mean}(x_0,y_0) + k_I I_{std}(x_0,y_0) \tag{5.12}$$

(10) Stop repeating the region growing procedure if in the last iteration no new pixels are added in the growing region or the region has overgrown the initial segmentation region.

The region growing procedure is performed when an eligible singularity and corresponding seed point and dual point are detected. The growing decision is based on wavelet transform coefficient magnitude in the scale where a singularity is detected and underlying mammogram.

Experimental Results

In this sub-section I show the performance of the proposed region growing algorithm using the cluster 1 from mammogram mdb223, MIAS database [130].

A benign microcalcification cluster is presented on Fig. 5.5 (a) with a squared detail microcalcification zoomed onto the cluster. Despite its smoothness, the zoomed microcalcification is properly detected in spatial – frequency localization algorithm.

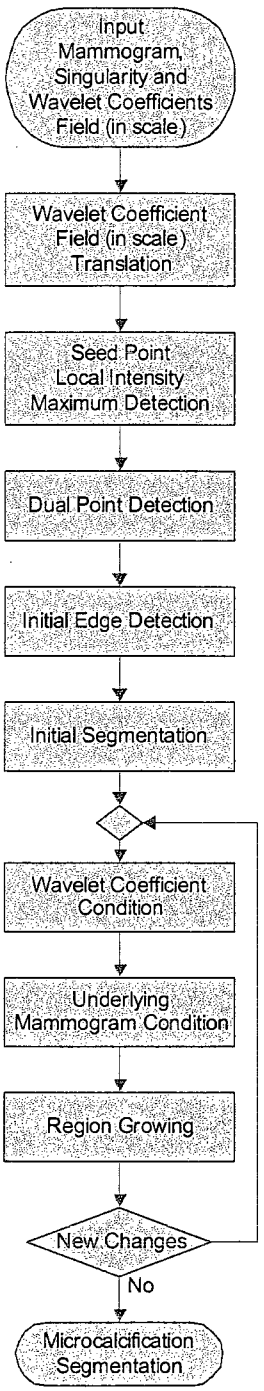

Figure 5.4. Region growing segmentation block diagram incorporated in the framework to further enhance the results

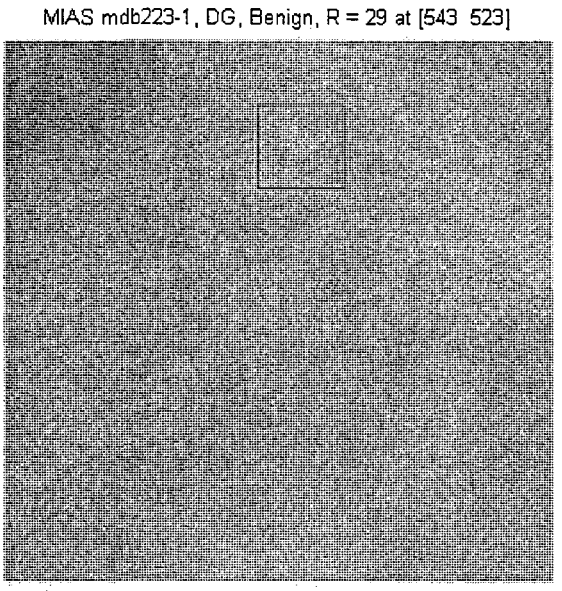

(a)

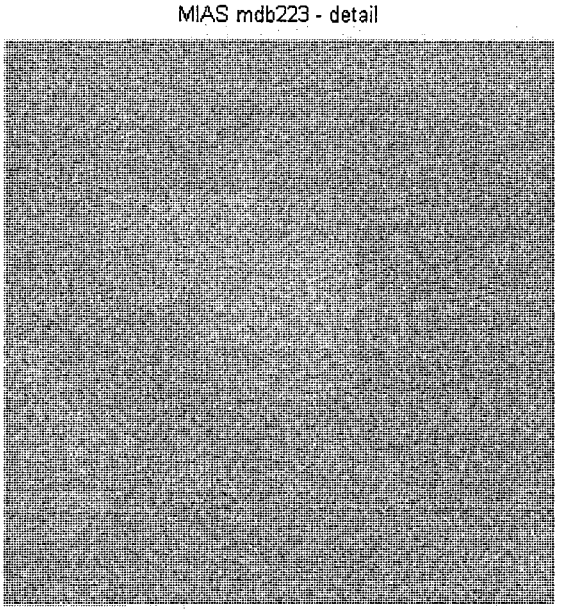

(b)

Figure 5.5. Mammogram mdb223, cluster 1 - (a) and microcalcification detail - (b)

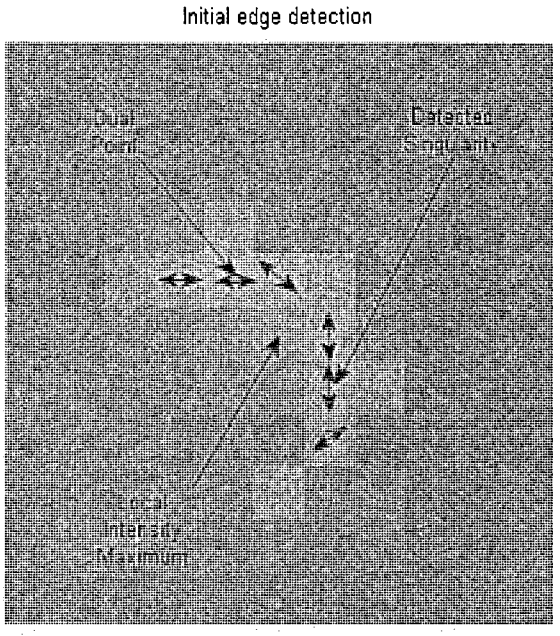

(a)

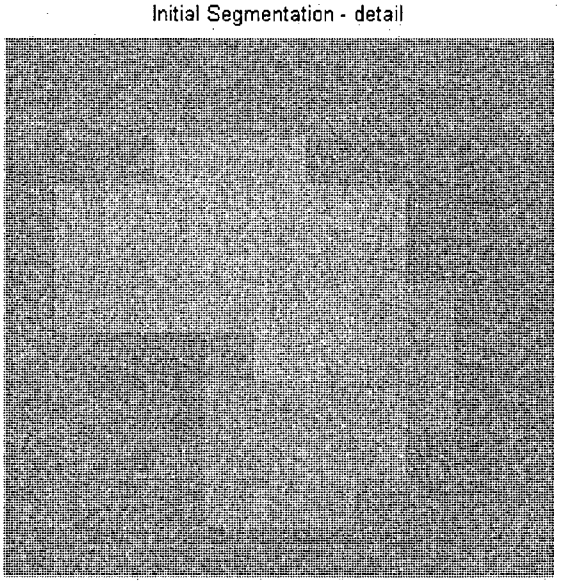

(b)

Figure 5.6. Mammogram mdb223, cluster 1 - detail with initial edge detection following wavelet coefficient argument from detected singularity and its dual point (a) and initial segmentation based on initial edge detection (b)

The detected singularity, local maximum, and the dual point of the zoomed microcalcification are shown on Fig. 5.6 – (a). Initial edge detection using formula (5.4) is highlighted on Fig. 5.6 – (a) with inserted arrows showing how the initial edges are constructed. Initial segmentation shown on Fig. 5.6 – (b) is the outer limit for the segmentation process.

Final segmentation is performed using the formulas (5.12) and (5.13). The resulting segmentation is shown on Fig. 5.7 – (a), while the zoomed detail is given on Fig. 5.7 – (b), showing that initially detected edges are preserved.

It is worth to say that the algorithm in Cluster 1, mammogram mdb223 initially found eligible 148 smoothed impulse functions with the average of 4.57×10^{-5}, while 49 were assigned as (above average) dominant singularities with the average 6.80×10^{-5}, requiring locally adaptive threshold technique. The high number of microcalcifications in the cluster increased the average of general modulus maxima and the local magnitude average leading to high false negative results. The proposed segmentation algorithm with just one constraint, local maximum presence, was able to significantly decrease false positive findings from total 148 to 86 with no magnitude threshold. Average threshold selected 49 findings with 37 false negative. Employing local intensity maximum of underlying mammogram, the algorithm has become less dependent on the threshold value which allows higher level of freedom in the election of lower general modulus maximum threshold.

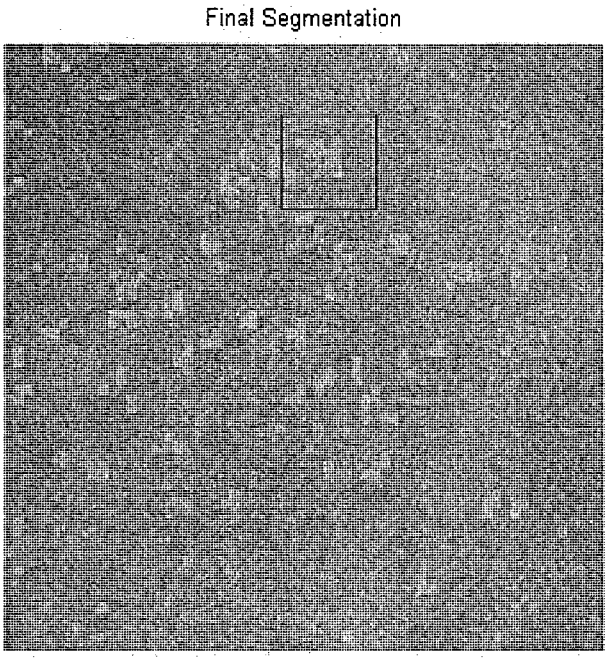

(a)

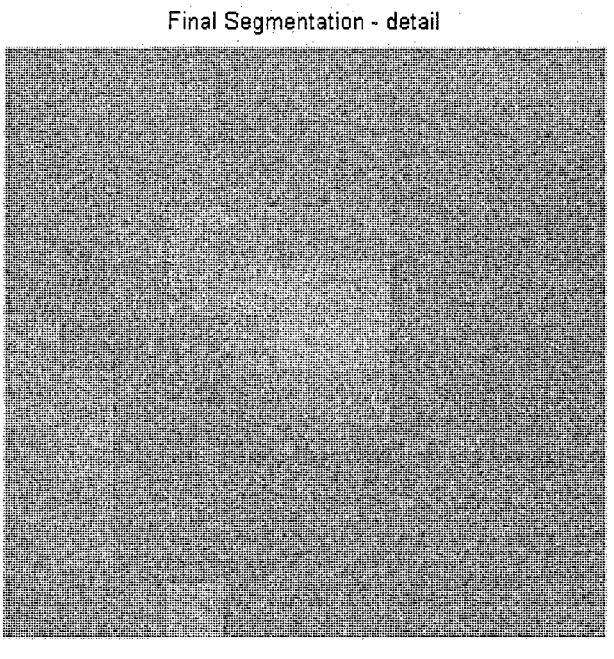

(b)

Figure 5.7. Mammogram mdb223, cluster 1- segmented image – (a) and segmented detail – (b)

Discussion

In this section I present how to employ detected singularity and local maximum as well as local wavelet coefficients i.e. their magnitudes and arguments to improve the proposed framework's performance.

The selection of dominant smoothed impulse function enabled detection of energy peaks which are the sign of a suspicious spot. The size of a suspicious spot can be estimated by an optimization technique that uses different filter sizes.

Desired high sensitivity of this detection algorithm combined with a non-adaptive threshold yields high false positive and false negative findings and thus low specificity becomes the most significant concern that need to be resolved if this algorithm to be put into practical use.

In this chapter, I showed that using additional knowledge about target I was able to decrease false findings significantly not compromising high sensitivity of the algorithm. In the case of microcalcifications appearing as spots brighter than their surroundings, performance was improved even with decreasing threshold.

This framework can be used to process any specific by adding more constraints. To generate a segmented image the modulus maxima values were incorporated into growing region segmentation process over several iterations. It is significant to emphasize that there was no pre-processing of any data nor there is any post-processing of results.

CHAPTER VI

CONCLUSIONS AND FUTURE WORK

Microcalcifications are residual calcium deposits that are often the first signs of developing breast abnormalities that may lead to breast cancer. Up to 30% of cancerous lesion in diagnosed breast cancer cases could have been detected earlier through mammogram screenings if the right tools were available. While the detection of calcifications may be easier in fatty backgrounds, it is challenging in dense parenchyma, suggesting the need for more sensitive tools for accurately identifying suspicious regions in mammograms and propping a computer-aided system for further target classification.

Summary and Conclusions

Continuous wavelet transform is employed to detect singularities in mammograms by tracking modulus maxima along maxima lines. This work is based on convolving the mammogram with Gaussian kernel to detect and extract microcalcifications that are modeled as smoothed impulse functions. Two significant characteristics of the local modulus maxima of the wavelet transform with respect to the smoothed impulse function are investigated: magnitude of general maximum and fractal dimension of the detected sets of singularities.

This detection approach is independent of the background tissue and is complementary to a computer-aided diagnosis system based on shape, morphology, and spatial distribution of individual microcalcifications.

Experimental work is performed on a set of images with empirically selected parameters for 200 μm/pixel spatial and 8 bits/pixel numerical resolution. Results are indicating that in abnormal regions the selected general maxima have larger magnitudes and tend to have higher fractal dimension than in surrounding normal regions. Findings are promising since they can be integrated into any framework for breast cancer detection and diagnosis.

Dissertation Contributions

This Dissertation has addressed the problem of singularity analysis in 2-D signals and its use for the microcalcification detection in mammograms. This work has the following contributions,

- Developed a tool that is able accurately to compute wavelet coefficients, detect singular points in a 2-D signal, and classify the detected singularities in accordance to their known properties.

- Showed that dominant general modulus maximum of the smoothed impulse function is a significant feature for microcalcification detection leading to both microcalcification cluster localization and microcalcification segmentation.

- Showed that general modulus maximum of smoothed impulse function can be modeled as a general framework that can be used independently or integrated with other microcalcification detection algorithms.

- Showed that the magnitudes of the general maxima of smoothed impulse functions are not sensitive on background tissue in mammogram, which is particularly important because microcalcification detection in dense parenchyma can be a very challenging task.

Future Work

A number of research projects can be pursued by carrying extension of this dissertation. An example of such are,

- Malignant clusters appeared with lower average of general modulus maxima than benign clusters', which implies that general modulus maximum related to a malignant microcalcification corresponds to lower scale than the scale of the general modulus maximum related to a benign one. The investigation of the scale and the shape of smoothed impulse function could improve detection of particularly malignant microcalcification clusters and hence this framework can be used as a diagnosis tool.

- The computed fractal dimension of detected smoothed impulse function supports the assumption that general modulus maximum feature preserves spatial distribution of microcalcifications, i.e. the areas with microcalcification clusters tend to have higher fractal dimension than

the healthy areas. Practical implementation of how to use fractal dimension in microcalcification detection and/or classification can be a significant of a future work.

- The overall system is computationally intensive that can be optimized and accelerated by using a multi-processor hardware. Real time processing during the screening procedure can be beneficiary in many ways. It will, reduce the amount of radiation a patient is exposed to, no need for an additional screening, and it would save the patients from having to endure the uncomfortable feelings during the procedure and more importantly, emotionally surviving cancer while waiting for additional test results. Real time implementation of this dissertation can be an interesting and challenging extension.

BIBLIOGRAPHY

[1] American Cancer Society. (2009). *Breast Cancer Facts and Figures 2007-2008.* Retrieved from http://www.cancer.org/downloads/stt/bcff-final.pdf.

[2] Zhou, X.H., and Gordon, R. (1989.). Detection of early breast cancer: an overview and future prospects. *Critical Reviews in Biomedical Engineering, 17(3)*, 203–255.

[3] Horner M.J., Ries L.A.G., Krapcho M., Neyman N., Aminou R., Howlader N., Altekruse S.F., Feuer E.J., Huang L., Mariotto A., Miller B.A., Lewis D.R., Eisner M.P., Stinchcomb D.G., and Edwards B.K. (Eds.) (2009). SEER Cancer Statistics Review, 1975-2006. *National Cancer Institute. Bethesda, MD*, Retrieved from http://seer.cancer.gov/csr/1975_2006

[4] Berry D.A., Cronin K.A., Plevritis S.K. Fryback, D.G., Clarke, L., Zelen, M., .. Feuer, E.J. (2005), Effect of screening and adjuvant therapy on mortality from breast cancer. *The New England Journal of Medicine, 353(17)*, 1784-1792.

[5] Giordano S.H., Cohen D.S., Buzdar A.U., Perkins G., and G.N. Hortobagyi. (2004). Breast carcinoma in men: a population-based study. *Cancer 101(1)*, 51-57.

[6] Heine J.J., and Malhotra P. (2002). Mammographic tissue, breast cancer risk, serial image analysis, and digital mammography. Part 1. Tissue and related risk factors. *Acad Radiol. 9(3)*, 298-316.

[7] Heine J.J., and Malhotra P. (2002). Mammographic tissue, breast cancer risk, serial image analysis, and digital mammography. Part 2. Serial breast tissue change and related temporal influences. *Acad Radiol. 9(3)*, 317-335.

[8] Kallergi M. (2004), Computer-aided diagnosis of mammographic microcalcification clusters. *Medical Physics, 31(2)*, 314-326.

[9] Heine J.J., Deans S.R., Cullers D. K., Stauduhar R., and Clarke L. P. (1997). Multiresolution Statistical Analysis of High-Resolution Digital Mammograms. *IEEE Transaction on Medical Imaging 16(5)*, 503-515.

[10] Tabar, L., Yen, M.F, Vitak, B., Tony Chen, H.H., Smith, R.A., and Duffy, S.W. (2003). Mammography service screening and mortality in breast cancer patients: 20-year follow-up before and after introduction of screening. *Lancet. 361(9367)*, 1405-1410.

[11] Friedrich, M. (1997). *Radiological Diagnosis of Breast Diseases* (M. Friedrich and E.A. Sickles, Eds). Berlin: Springer.

[12] Kerlikowske, K., and Barclay, J. (1997). Outcomes of modern screening mammography. *J. Natl. Cancer. Inst. Monogr. 22*, 105-111.

[13] Eklund, G.W. (1997). *Radiological Diagnosis of Breast Diseases* (M. Friedrich and E.A. Sickles, Eds). Berlin: Springer.

[14] Giger, M.L., Lu, P., Huo, Z., Bick, U., Vyborny, C.J., Schmidt, R.A., Zhang, W., Metz, C.E., Wolverton, D., Nishikawa, R.M., Zouras, W. and Doi, K. (1994). CAD in Digital Mammography: Computerized Detection and Classification of Masses. *International Workshop on Digital Mammography, York, England*, 281-287.

[15] Miller, P., and Astley, S. (1993). Automated Detection of Mammographic Aymmetry using Anatomical Features. *International Journal of Pattern Recognition and Artificial Intelligence 7(6)*, 1461-1476.

[16] Liszka, G., Roska, T., Zarandy, A., Hegyesi, J., Kek, L.,and Rekeczky, C. (1995). Mammogram analysis using CNN algorithms. *SPIE, 2434*, 461-470.

[17] GE Healthcare. (2009). *Senographe 2000D Full-Field Digital Mammography systems*. Retrieved from http://www.gehealthcare.com/rad/whc/products/mswh2000d.html

[18] Takeda, T., Momose, A., and Hirano, K. (2000). Human carcinoma: Early experience with phase-contrast x-ray CT with synchrotron radiation - comparative specimen study with optical microscopy. *Radiology, 214*, 298-301.

[19] Tanaka, T. Honda, C., Matsuo, S., Noma, K., Oohara, H., Nitta, N., .. Murata, K. (2005). The First Trial of Phase Contrast Imaging for Digital Full-Field Mammography Using a Practical Molybdenum X-Ray Tube. *Investigative Radiology, 40(7)*, 385-396.

[20] Skaane. P., and Skjennald A. (2004). Screen-film mammography versus full-field digital mammography with soft-copy reading: randomized trial in a population-based screening program - The Oslo II Study. *Radiology, 232*, 197-204.

[21] Wright, G.A. (1997). Magnetic Resonance Imaging. *IEEE Signal Processing Magazine, 1*, 56-66.

[22] Heywang, S.H., Hahn, D., Schmidt, H., Krischke, I., Eiermann, W., Bassermann, R., and Lissner, J. (1986). MR Imaging of the Breast using Gadolinium-DTPA. *Journal of Computer Assisted Tomography, 10(2)*, 199-204.

[23] Watson, A.D. (1995). *MRI for Technologists* (P. Woodward, and R.D. Freimarck, Eds.). McGraw-Hill.

[24] Zuo, C.S., Jiang, A. Buff, B.L., Mahon, T.G., and Wong, T.Z. (1996). Automatic Motion Correction for Breast MR Imaging. *Radiology, 198(3)*, 903-906.

[25] Lohmann, G. (1998). *Volumetric Image Analysis*. John Wiley & Sons.

[26] Heywang, S.H., Lipsit, E.R., and Glassman, L.M. (1984). Specficity of ultrasonography in the diagnosis of benign breast masses. *J. Utrasound AIFD 3*, 453-461.

[27] Calderon, C., Vikomerson, D., and Mezrich, R. (1976). Differences in attenuation for ultrasound by normal, benign, and malignant breast tissue. *J. Clin. Utrasound, 4*, 249-254.

[28] Zonderland, H.M. Coerkamp, E.G., Hermans, J., Van de Vijver, M.J., and Van Voorthuisen, A.E. (1999). Diagnosis of breast cancer: contribution of US as an adjunct to mammography. Radiology 213(2), 413-422.

[29] Yang, W.T., Suen, M., Ahuja, A., and Meterweli, C. (1997). In vivo demonstration of microcalcification in breast cancer using high resolution ultrasound. The British Journal of Radiology, 70(835) 685–690.

[30] Xiao, G., Brady, J. M., Noble, J. A., Burcher, M., and English, R. (2002). Nonrigid Registration of 3-D Free-Hand Ultrasound Images of the Breast. *IEEE Transaction on Medical Imaging, 21(4)*, 405-412.

[31] Huang, S.F., Chang, R.F., Chen, D.R., and Moon, W.K. (2004). Characterization of Spiculation on Ultrasound Lesions. *IEEE Transaction on Medical Imaging, 23(1)*, 111-121.

[32] Fear, E., Sill, J., and Stuchly, M. (2003). Experimental Feasibility Study of Confocal Microwave Imaging for Breast Tumor Detection. *IEEE Transaction on Microwave Theory and Techniques, 51(3)*, 887-897.

[33] Bindu, G., Abraham, S. J., Lonappan, A., Thomas, V., Aanandan, C. K., and Mathew, K. T. (2005). Effects of reduced contrast coupling medium in microwave breast imaging. Wiley Periodicals, Inc. Microwave Optical Technology Letters, 47(5), 443-446.

[34] Bindu, G., Lonappan, A., Thomas, V., Aanandan, C., and Mathew, K.T. (2006). Active Microwave Imaging for Breast Cancer Detection. *Progress In Electromagnetic Research, PIER 58*, 149-169.

[35] Li, D., Meaney, P.M., and Paulsen, K.D. (2003). Conformal microwave imaging for breast cancer detection. *IEEE Transactions on Microwave Theory and Techniques 51(4)*, 1179-1186

[36] Beam, C., Layde, P., and Sullivan, D. (1996). Variability in the interpretation of screening mammograms by US radiologists, findings from a national sample. *Archives of Internal Medicine, 156(2)*, 209-213.

[37] Elmore, J. G., Miglioretti, D. L., Reisch, L. M., Barton, M. B., Kreuter, W., Christiansen, C. L., and Fletcher, S. W. (2002). Screening mammograms by community radiologists: Variability in false-positive rates. *Journal of the National Cancer Institute 94(18)*, 1373-1380.

[38] Giger, M.L., Karssemeijer, N., and Armato, S.G. (2001). Guest editorial computer-aided diagnosis in medical imaging. IEEE Transactions on Medical Imaging, 20(12), 1205-1208

[39] Dengler, J., Behrens, S., and Desaga, J.F. (1993). Segmentation of microcalcifications in mammograms. *IEEE Transactions on Medical Imaging, 12(4)*, 634-642.

[40] Cheng, H.D., Cai, X., Chen, X., Hu, L., and Lou, X. (2003). Computer-aided detection and classification of microcalcifications in mammograms: a survey, *Pattern Recognition, 36*, 2967 – 2991.

[41] Zhang, W., Yoshida, H., Nishikawa, R. M., and Doi, K. (1998). Optimally weighted wavelet transform based on supervised training for detection of microcalcifications in digital mammograms. *Medical Physics, 25(6)*, 949-956.

[42] ImageChecker R2 Technology. (2009). Retrieved from http://rsna2005.rsna.org/rsna2005/V2005/exhibitor_list/displayEx.cvn?exbID=966 and http://www.hologic.com/breast-screening/imagechecker

[43] Diekmann, F., Diekmann, S., Jeunehomme, F., Muller, S., Hamm, B., and Bick, U. (2005). Digital mammography using iodine-based contrast media: Initial clinical experience with dynamic contrast medium enhancement. *Investigative Radiology, 40(7),* 397–404

[44] Russ, J.C. (2007). *The Image Processing Handbook.* Boca Raton: CRC Press.

[45] Bakic, P.R., and Brzakovic, D.P. (1997). Applications of Neural Networks to Diagnosing Breast Cancer. *5th Seminar on Neural Network Applications.* Belgrade.

[46] Stewart, B.D., Folkes, D.A., Cairns, A.Y., Ricketts, I.W., Preece, P.E., and Thompson, A.J. (1992). Computer Image Processing in Mammographic Screening: A Review. *Automedica, 15*, 23-45.

[47] Woods, K., Clarke, L.P., and Velthuizen R. (1991). Enhancement of digital mammograms using a local thresholding technique. *Annual International Conference of the IEEE Engineering in Medicine and Biology Society 13(1)*, 114–115.

[48] Gordon, R., and Rangayyan, R.M. (1984). Feature enhancement of film mammograms using fixed and adaptive neighborhoods. *Applied Optics, 23 (4)*, 560-564.

[49] Dhawan, A.P., Buelloni, G., and Gordon, R. (1986). Enhancement of mammographic features by optimal adaptive neighborhood image processing, *IEEE Transaction on Medical Imaging 5(1)*, 8-15.

[50] Morrow, W.M., Paranjape, R.B., Rangayyan, R.M., and Desautels, J.E.L. (1992). Region-based contrast enhancement of mammograms. *IEEE Transactions on Medical Imaging, 11(3)*, 392-406.

[51] Gurcan, M.N., Yardimci, Y., Cetin, A.E., and Ansari, R. (1997). Detection of microcalcifications in mammograms using higher order statistics. *Signal Processing Letters, 4(8)*, 213-216.

[52] Gurcan, M.N., Yardimci, Y., Cetin, A.E., and Ansari, R. (1997). Automated detection and enhancement of microcalcifications in mammograms using nonlinear subband decomposition. *IEEE International Conference on Acoustics, Speech, and Signal Processing, 4*, 3069-2072.

[53] Cheng, H.D., Lui, Y.M., and Freimanis, R.I. (1998). A novel approach to microcalcification detection using fuzzy logic technique. *IEEE Transaction on Medical Imaging, 17(3)*, 442-450.

[54] Laine, A.F., Schuler, S., Fan, J., and Huda, W. (1994). Mammographic feature enhancement by multiscale analysis. *IEEE Transactions on Medical Imaging, 13(4)*, 7250-7260.

[55] Li, H., Ray Liu, K.J., Lo, S.C.B. (1997). Fractal modeling and segmentation for the enhancement of microcalcifications in digital mammograms. *IEEE Transaction Medical Imaging 16(6)*, 785-798.

[56] Davies, D.H., and Dance, D.R. (1992). The automatic computer detection of subtle calcifications in radiographically dense breasts. *Physics in Medicine and Biology, 37*, 1385-1390.

[57] Karssemeijer, N. (1993). Adaptive noise equalization and recognition of microcalcification clusters in mammograms, *International Journal of Pattern Recognition and Artificial Intelligence, 7(6)*, 1357-1376.

[58] Veldkamp, W.J.H., and Karssemeijer, N. (2000). Normalization of local contrast in mammograms. *IEEE Transaction on Medical Imaging, 19(7)*, 731-738.

[59] Zhang, X.P., and Desai, M.D. (2001). Segmentation of bright targets using wavelets and adaptive thresholding. *IEEE Transaction on Image Processing, 10(7)*, 1020-1030.

[60] Kim, J.K. Park, J.M. Song, S.S., and Park, H.W. (1998). Detection of clustered microcalcifications on mammograms using surrounding region dependence method and artificial neural network. *The Journal of VLSI Signal Processing, 18(3)*, 251-262.

[61] Wallet, B.C., Solka, J.L., and Priebe, C.E. (1997). A method for detecting microcalcifications in digital mammograms. *Journal of Digital Imaging 10(3)*, 136-139.

[62] Qian, W., Clarke, L.P., Kallergi, M., and Clark, R.A. (1994). Tree-structured nonlinear filters in digital mammography. *IEEE Transaction on Medical Imaging, 13(1)*, 25-36.

[63] Dippel, S., Stahl, M., Wiemker, R., and Blaffert, T. (2002). Multiscale contrast enhancement for radiographies: Laplacian pyramid versus fast wavelet transform, *IEEE Transaction on Medical Imaging, 21(4)*, 343-353.

[64] Netsch, T., and Peitgen, H.O. (1999). Scale-space signatures for the detection of clustered microcalcifications in digital mammograms. *IEEE Transaction on Medical Imaging, 18(9)*, 774-786.

[65] Strickland, R.N., and Hahn, H.I. (1997). Wavelet transform methods for object detection and recovery. IEEE Transactions on Medical Imaging 6(5), 724-735.

[66] Li, H., Liu, K.J. R., and Lo, S.C.B. (1997). Fractal modeling and segmentation for the enhancement of microcalcifications in digital mammograms. *IEEE Transaction on Medical Imaging 16(6)*, 785-798.

[67] Bothorel, S., Meunier, B.B., and Muller, S. (1997). A fuzzy logic based approach for semiological analysis of microcalcifications in mammographic images. *International Journal of Intelligent Systems 12(11-12)*, 819–848.

[68] Cheng, H.D., Chen, J.R., Freimanis, R.I., and Jiang, X.H. (1998). A novel fuzzy logic approach to microcalcification detection, *Elesevier Information Sciences, 111(1)*, 189-205.

[69] Yu, S., Guan, L., and Brown, S. (1999). Automatic detection of clustered microcalcifications in digitized mammogram films. *J. Electronic Imaging, 8(01)*, 76-82.

[70] Yu, S., and Guan, L. (2000). A CAD system for the automatic detection of clustered microcalcifications in digitized mammogram films. *IEEE Transactions on Medical Imaging, 19(2)*, 115-126.

[71] Davies, D.H., and Dance, D.R. (1990). Automatic computer detection of clustered calcifications in digital mammograms. *Physics in Medicine and Biology, 35*, 1111-1118.

[72] Karssemeijer, N. (1993). Recognition of microcalcification clusters in mammograms, International Journal of Pattern Recognition and Artificial Intelligence 7(6), 1357-1376.

[73] Karahaliou, A., Skiadopoulos, S., Boniatis, I., Sakellaropoulos, P., Likaki, E., Panayiotakis, G., and Costaridou, L. (2007). Texture analysis of tissue surrounding microcalcifications on mammograms for breast cancer diagnosis. *The British Journal of Radiology, 80*, 648-656.

[74] Lyra, M., Lyra, S., Kostakis, B., Drosos, S., Georgosopoulos, C., and Skouroliakou, K. (2008). Digital mammography texture analysis by computer assisted image processing. *IEEE International Workshop on Imaging Systems and Techniques*, 73-76.

[75] Dhawan, A.P., Chitre, Y., Kaiser-Bonasso, C., and Moskowita, M. (1996). Analysis of mammographic microcalcifications using grey-level image structure features. *IEEE Transactions on Medical Imaging, 15(3)*, 246-259.

[76] Kim, J.K., and Park, H.W. (1999). Statistical textural features for detection of microcalcifications in digitized mammograms. *IEEE Transactions on Medical Imaging, 18(3)*, 231-238.

[77] Geronimo, J.S., Hardin, D.P., and Massopust, P.R. (1994). Fractal functions and wavelet expansions based on several scaling functions, *Journal of Approximation Theory, 78*, 373-401.

[78] Chang, T., and Jay Kuo, C.C. (1993). Texture analysis and classification with tree-structured wavelet transform. *IEEE Transactions on Image Processing, 2(4)*, 429-441.

[79] Laine, A., and Fan, J. (1993). Texture classification by wavelet packet signatures. *IEEE Transactions on Pattern Analysis and Machine Intelligence, 15(11)*, 1186-1191.

[80] Mallat, S. G. (1989). A theory for multiresolution signal decomposition: the wavelet representation. *IEEE Transactions on Pattern Analysis and Machine Intelligence, 11*, 674-693.

[81] Pikaz, A., and Averbuch, A. (1997). An efficient topological characterization of gray-levels textures, Using a Multiresolution Representation. *Graphical Models and Image Processing, 59(1)*, 1–17.

[82] Tsai, D. M., and Hsiao, B. (2001). Automatic surface inspection using wavelet reconstruction. *Pattern Recognition 34*, 1285-1305

[83] Dhawan, A.P., Chitre, Y., Bonasso, C., and Wheeler, K. (1995). Radial-basis-function based classification of mammographic microcalcifications using texture features. Proceedings from *The 1995 IEEE Engineering in Medicine and Biology 17th Annual Conference and 21st Canadian Medical and Biological Engineering Conference*, 535-536.

[84] Chan, H.P., Doi, K., Galhotra, S., Vyborny, C.J., MacMahon, H., and Jokich, P.M. (1987). Image feature analysis and computer-aided diagnosis in digital radiography I. Automated detection of microcalcifications in mammography. *Medical Physics 14(4)*, 538-548.

[85] Zhang, L., Qian, W., Sankar, R., Song, D., and Clark, R. (2001). A new false positive reduction method for MCCs detection in digital mammography, Proceedings from *IEEE International Conference on Acoustics, Speech and Signal Processing*, 1033-1036.

[86] Cordella, L.P., Tortorella, F., and Vento, M. (2000). Combing experts with different features for classifying clustered microcalcifications in mammograms, Proceedings from *15th International Conference on Patten Recognition*, 324-327.

[87] Nishlkawa, R.M., Giger, M.L., Dio, K., Vyborny, C.J., and Schmidt, R.A. (1993). Computed-aided detection of clustered microcalcifications: an improved method for grouping detected signals. *Medical Physics 20(6)*, 1661-1666.

[88] Kocur, C.M., Rogers, S.K., Myers, L.R., Burns, T., Kabrisky, M., Hoffmeister, J.W., Baver, K.W., and Steppe, J.M. (1996). Using neural networks to select wavelet features for breast cancer diagnosis. *IEEE Engineering in Medicine and Biology Magazine, 15(3)*, 95-102.

[89] Dhawan, A.P., Chitre, Y.S., Moskowitz, M., and Gruenstein, E. (1991). Classification of mammographic microcalcification and structural features using an artificial neural network. Proceedings from *The Annual International*

Conference of the IEEE Engineering in Medicine and Biology Society, 13(3), 1105-1106.

[90] Chitre, Y.S., Dhawan, A.P., and Moskowitz, M. (1993). Artificial neural network based classification of mammographic microcalcifications using image structure and cluster features. Proceedings from *The Annual Conference on Engineering in Medicine and Biology, 15*, 298-309.

[91] Mencattini, A., Rabottino, G., Salmeri, M., Caselli, F., Lojacono, R., and Frondizi, G. (2008). Features extraction to classify microcalcification clusters in mammography. Proceedings from *16th IMEKO TC4 Symposium Exploring New Frontiers of Instrumentation and Methods for Electrical and Electronic Measurements*. Florence, Italy.

[92] Lee, C.S., Kim, J.K., and Park, H.W. (1998). Computer-aided diagnostic system for breast cancer by detecting microcalcification. Proceedings from *SPIE Image Display Conference, 3335*, 615-626.

[93] Verma, B., and Zakos, J. (2001). A computer-aided diagnosis system for digital mammograms based on fuzzy-neural and feature extraction techniques. *IEEE Transactions on Informational Technology in Biomedicine, 5(1)*, 46–54.

[94] Dhawan, A.P., Chitre, Y.S., and Moskowitz, M. (1993). Artificial neural network based classification of mammographic microcalcifications using image structure features, Proc. SPIE 1905 (1993) 820-831.

[95] Gurcan, M.N., Chan, H.P., Sahiner, B., Hadjiiski, L., Petrick, N., and Helvie, M.A. (2002). Optimal neural network architecture selection: improvement in computerized detection of microcalcifications. *Academic Radiology, 9(4)*, 420-429.

[96] Gurcan, M.N., Sahiner, B., Chan, H.P., Hadjiiski, L., and Petrick, N. (2001). Selection of an optimal neural network architecture for computer-aided detection of microcalcifications—comparison of automated optimization techniques. *Medical Physics, 28(9)*, 1937-1948.

[97] Sahiner, B., Chan, H.P., Petrick, N., Helvie, M.A., and Goodsitt, M.M. (1998). Design of a high-sensitivity classifier based on a genetic algorithm: application to computer-aided diagnosis. *Physics in Medicine and Biology, 43*, 2853-2871.

[98] Anastasio, M.A., Yoshida, H., Nagel, R., Nishikawa, R.M., and Doi, K. (1998). A genetic algorithm-based method for optimizing the performance of a computer-aided diagnosis scheme for detection of clustered microcalcifications in mammograms. *Medical Physics, 25(9)*, 1613-1620.

[99] Chan, H.P., Sahiner, B., and Lam, K.L., Petrick N., Helvie M.A., Goodsitt, M.M., and Adler, D.D. (1998). Computerized analysis of mammographic microcalcifications in morphological and texture features space. *Medical Physics, 25(10)*, 2007-2019.

[100] Kramer, D., and Aghdasi, F. (1998). Classification of microcalcifications in digitized mammograms using multiscale statistical texture analysis. Proceedings from *The South African Symposium on Communications and Signal Processing*, 121-126.

[101] Zadeh, H.S., Nezhad, S.P., and Rad, F.R. (2001). Shape-based and texture-based feature extraction for classification of microcalcification in mammograms, Proc. SPIE 4322 (2001) 301–310.

[102] Kramer, D., and Aghdasi, F. (1999). Texture analysis techniques for the classification of microcalcifications in digitized mammograms. Proceedings of *The 1999 Fifth IEEE AFRICON Conference Electrotechnical Service for Africa*, 395-400.

[103] Woods, K.S., Doss, C.C., Bowyer, K.W. Solka, J.L., Priebe, C.E., and Kegelmeyer, W.P. (1993). Comparative evaluation of pattern recognition techniques for detection of microcalcifications in mammography. *International Journal of Pattern Recognition and Artificial Intelligence, 7*, 1417-1436.

[104] Zheng, L., and Chan, A.K. (2001). An artificial intelligent algorithm for tumor detection in screening mammogram. *IEEE Transactions on Medical Imaging, 20(17)*, 559-567.

[105] Li, H.D., Kallergi, M., Clarke, L.P., Jain, V.K., and Clark, R.A. (1995). Markov random field for tumor detection in digital mammography. IEEE Transactions on Medical Imaging, 14(3), 565-576.

[106] Lyer, N.S., Kandel, A., and Schneider, M. (2000). Feature-based fuzzy classification for interpretation of mammograms. *Fuzzy Sets and Systems, 114(2)*, 271-280.

[107] Hall, L.O. (1996). Learned fuzzy rules versus decision trees in classifying microcalcifications in mammograms. Proceedings from SPIE, 2761, 54-61. Orlando, FL.

[108] Wang, T. C., and Karayiannis, N. B. (1998). Detection of microcalcifications in digital mammograms using wavelets. *IEEE Transactions on Medical Imaging, 17(4)*, 498-509.

[109] Mallat, S., and Hwang, W. L. (1992). Singularity detection and processing with wavelets. *IEEE Transactions on Information Theory, 38(2)*, 617-643.

[110] Mallat, S., and Zhong, S. (1992). Characterization of signals from multiscale edges. *IEEE Transactions on Pattern Analysis and Machine Intelligence, 14(7)*, 710-732.

[111] Mallat, S. (1999). *A wavelet tour of signal processing*, Academic Press.

[112] Meyer, Y. (1991). Un contre-exemple à la conjecture de Marr et celle de S. Mallat. Preprint.

[113] Bruce, L. M., and Adhami, R. R. (1999). Classifying mammographic mass shapes using the wavelet transform modulus-maxima method. *IEEE Transactions on Medical Imaging, 18(12)*, 1170-1177.

[114] Tang, Y. Y., Yang, L., and Liu, J. (2000). Characterization of Dirac-structure edges with wavelet transform. *IEEE Transaction on Systems, Man, and Cybernetics — Part B: Cybernetics, 30(1)*, 93-109.

[115] Lemaur, G., Drouiche, K., and DeConinck, J. (2003). Highly regular wavelets for the detection of clustered microcalcifications in mammograms. *IEEE Transactions on Medical Imaging, 22(3)*, 393-401.

[116] I. Daubechies, Orthogonal bases of compactly supported wavelets, Commun. Pure Appl. Math., vol. 41, pp. 909–996, 1988.

[117] Witkin, A. P. (1983). Scale-space filtering. Proceedings from 8th International Joint Conference Artificial Intelligence, 1019-1022. Karlsruhe, Germany.

[118] Young, R. A. (1987). The Gaussian derivative model for spatial vision: I. Retinal mechanisms. *Spatial vision, 2(4)*, 273-293.

[119] DeAngelis, G. C., Ozawa, I., and Freeman, R. D. (1995). Receptive-field dynamics in the central visual pathways. *Trends in Neurosciences, 18*, 451-458.

[120] Strickland, R. N., and Hahn, H. I. (1996). Wavelet transforms for detecting microcalcifications in mammograms. *IEEE Transactions on Medical Imaging, 15()2*, 218-229.

[121] Lindberg, T. (1998). Edge detection and ridge detection with automatic scale selection. *International Journal of Computer Vision, 30 (2)*, 117-154.

[122] Lindberg, T. (1998). Feature detection with automatic scale selection, *International Journal of Computer Vision, 30 (2)*, 79-116.

[123] Arneodo, A., Bacry, E., and Muzy, J. F. (1995). The thermodynamics of fractals revisited with wavelets. *Physica A, 213*, 232-275.

[124] Arneodo, A., Audit, B., Bacry, E., Manneville, S., Muzy, J. F., and Roux, S. G (1998). Thermodynamics of fractal signals based on wavelet analysis: application to fully developed turbulence data and DNA sequences. *Physica A, 254*, 24-45.

[125] Decoster, N. (1999). *Analyse multifractale d'images de surfaces rigueuses à l'aide de la transformation en ondolettes*, L'Université de Bordeaux I. Retrieved from http://decoster.free.fr/phd.

[126] Arneodo, A., Decoster, N., and Roux, S.G. (2000). A wavelet-based method for multifractal image analysis. I. Methodology and test applications on isotropic and anisotropic random rough surfaces. *The European Physical Journal B, 15(3)*, 567-600.

[127] Kestener, P. (2003). *Analyse multifractale 2D et 3D a l'aide da la transformation en ondolettes: application en mammography et en turbulence developpée (These)*. L'Univeristé Bordeaux I, Ecole Doctorale de Sciences Physiques et de l'Ingenieur. Retrieved from http://tel.archives-ouvertes.fr/docs/00/04/58/55/PDF/tel-00004013.pdf

[128] Roux, S., Muzzy, J. F., and Arneodo, A. (1999). Detecting vorticity filaments using wavelet analysis: About the statistical contribution of vorticity filaments to intermittency in swirling turbulent flows. *The* European *Physical Journal B, Condensed matter* physics, *8(22)*, 301-322.

[129] Mandelbrot, B. (1967). How long is the coast of Britain? Statistical self-similarity and fractional dimension, *Science, New Series, 156(3775)*, 636-638.

[130] Suckling, J., et al. (1994). The Mammographic Image Analysis Society Digital Mammogram Database. *Exerpta Medica International Congress, 1069*, 375-378. Retrieved from http://peipa.essex.ac.uk/info/mias.html.

[131] Reinhard, E., Ward, G., Pattanaik, S., and Debevec, P. (2006). *High Dynamic Range Imaging: Acquisition, Display, and Image-Based Lighting*, The Morgan Kaufmann Series in Computer Graphics and Geometric Modeling, Elsevier.

[132] Bujanovic, T., and Abdel-Qader, I. (2009). On wavelet transform general modulus maxima metric for microcalcification detection, *in print.*

[133] Abdel-Qader, I., and Bujanovic, T. (2005). An integrated dynamic scene algorithm for segmentation and motion estimation. *EURASIP Journal on Applied Signal Processing, 12*, 1845-1853.